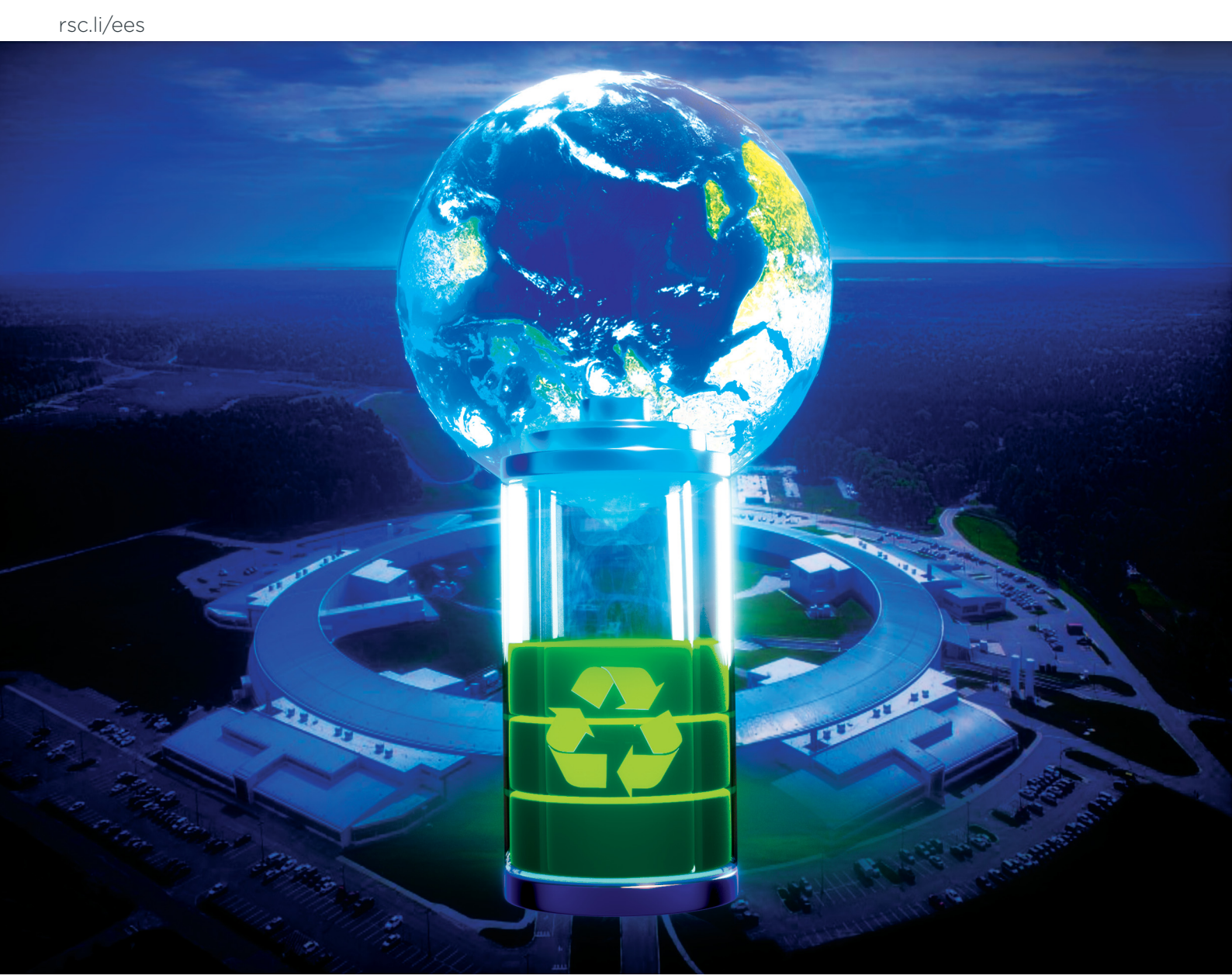
# Volume 16 Number 6 June 2023 Pages 2371-2708

# Energy & Environmental Science



ISSN 1754-5706



### **PAPER**

Varun Kankanallu, Mingyuan Ge, Karen Chen-Wiegart et al. Elucidating a dissolution-deposition reaction mechanism by multimodal synchrotron X-ray characterization in aqueous  $\rm Zn/MnO_2$  batteries

# Energy & Environmental Science



### PAPER



Cite this: Energy Environ. Sci.. 2023, 16, 2464

# Elucidating a dissolution-deposition reaction mechanism by multimodal synchrotron X-ray characterization in aqueous Zn/MnO2 batteries†

Varun R. Kankanallu, Da Xiaoyin Zheng, Denis Leschev, Nicole Zmich, Charles Clark, a Cheng-Hung Lin, ab Hui Zhong, Sanjit Ghose, Sanjit Ghos Andrew M. Kiss, D Dmytro Nykypanchuk, Eli Stavitski, D Esther S. Takeuchi, aefg Amy C. Marschilok, aefg Kenneth J. Takeuchi, aefg Jianming Bai, Mingyuan Ge\*b and Yu-chen Karen Chen-Wiegart\*ab

Aqueous Zn/MnO2 batteries with their environmental sustainability and competitive cost, are becoming a promising, safe alternative for grid-scale electrochemical energy storage. Presented as a promising design principle to deliver a higher theoretical capacity, this work offers fundamental understanding of the dissolution-deposition mechanism of  $Zn/\beta$ -MnO<sub>2</sub>. A multimodal synchrotron characterization approach including three operando X-ray techniques (powder diffraction, absorption spectroscopy, and fluorescence microscopy) is coupled with elementally resolved synchrotron X-ray nano-tomography. Together they provide a direct correlation between structural evolution, reaction chemistry, and 3D morphological changes. Operando synchrotron X-ray diffraction and spectroscopy show a crystalline-to-amorphous phase transition. Quantitative modeling of the operando data by Rietveld refinement for X-ray diffraction and multivariate curve resolution (MCR) for X-ray absorption spectroscopy are used in a complementary fashion to track the structural and chemical transitions of both the long-range (crystalline phases) and short-range (including amorphous phases) ordering upon cycling. Scanning X-ray microscopy and full-field nanotomography visualizes the morphology of electrodes at different electrochemical states with elemental sensitivity to spatially resolve the formation of the Zn- and Mn-containing phases. Overall, this work critically indicates that for Zn/MnO<sub>2</sub> aqueous batteries, the reaction pathways involving Zn-Mn complex formation upon cycling become independent of the polymorphs of the initial electrode and sheds light on the interplay among structural, chemical, and morphological evolution for electrochemically driven phase transitions.

Received 18th November 2022, Accepted 19th April 2023

DOI: 10.1039/d2ee03731a

rsc.li/ees

### **Broader context**

Due to the increasing demands of safety requirements, aqueous Zn/MnO<sub>2</sub> batteries have attracted great attention as promising candidates for next generation grid-scale energy storage systems. However, further understanding of the reaction mechanisms and proposing fundamental strategies to enhance the performances in Zn/MnO<sub>2</sub> batteries remain a crucial aspect towards employing these batteries for practical applications. This work offers fundamental understanding of the dissolution-deposition mechanism of Zn/β-MnO<sub>2</sub>. The key motivation of this work is twofold. First, this study highlights fundamental understanding of one of the most promising aqueous battery systems for all polymorphs in the mild-aqueous pH regime - namely, once the dissolution of the active material occurs in the first cycle the deposited phase is independent of the initial electrode present. This offers great potential for the future design of suitable electrode architecture for realization of safe, economical, and sustainable large-scale electrochemical energy storage. Second, the multimodal synchrotron characterization will be of great interest for all areas dealing with complex electrochemically driven phase transformation: combining operando analysis with different matter interaction and contrast mechanisms, across different length scales, can uniquely provide a deeper understanding on the coupling between structural evolution, reaction chemistry, and morphological changes.

a Department of Materials Science and Chemical Engineering, Stony Brook University, Stony Brook, NY, 11794, USA. E-mail: Karen.Chen-Wiegart@stonybrook.edu

<sup>&</sup>lt;sup>b</sup> National Synchrotron Light Source II, Brookhaven National Laboratory, Upton, NY, 11973, USA. E-mail: mingyuan@bnl.gov

<sup>&</sup>lt;sup>c</sup> Center for Functional Nanomaterials, Brookhaven National Laboratory, Upton, NY, 11973, USA

<sup>&</sup>lt;sup>d</sup> Department of Joint Photon Sciences Institute, Stony Brook University, NY, 11790, USA

<sup>&</sup>lt;sup>e</sup> Energy and Photon Sciences Directorate, Brookhaven National Laboratory, Upton, NY, 11973, USA

f Department of Chemistry, Stony Brook University, Stony Brook, NY, 11794, USA

g Institute of Energy Sustainability and Equity, Stony Brook University, Stony Brook, NY, 11794, USA

<sup>†</sup> Electronic supplementary information (ESI) available. See DOI: https://doi.org/10.1039/d2ee03731a

### 1. Introduction

Rechargeable aqueous batteries have the potential for largescale electrochemical energy storage devices owing to their safety, low cost, and sustainable chemicals. 1,2 Among various systems with different chemistries, the rechargeable Zn aqueous battery in comparison to the Li-ion battery has many advantages including the use of environmentally benign materials in the battery design and cost-effective manufacturing.<sup>3</sup> Zinc metal has a low redox potential (-0.76 V vs. SHE) and a high theoretical capacity (820 mA  $g^{-1}$ , 5851 A h  $L^{-1}$ ), which makes it an appealing air-stable battery anode with the prospect of high energy density.4 Zinc-manganese dioxide (Zn/MnO<sub>2</sub>) batteries have dominated the primary battery market owing to their low cost and safety. These implement an alkaline electrolyte which forms an irreversible complex during its operation which hinders its reversibility. Under alkaline conditions, the battery undergoes a single electron redox at the cathode to form manganese oxyhydroxide (MnOOH).5 On the other hand, Zn/MnO<sub>2</sub> batteries in mild aqueous electrolyte have demonstrated promising results due to its reversibility.<sup>6,7</sup> However, the further improvement of the Zn/α-MnO<sub>2</sub> battery performance is limited by capacity fade and low cycle life due to the formation of irreversible side products and active material dissolution. Further, understanding the reaction mechanisms and proposing fundamental strategies to enhance the performance of Zn/MnO<sub>2</sub> batteries with different MnO<sub>2</sub> polymorphs, remain a crucial aspect towards employing these batteries for practical applications.

Different reaction mechanisms have been proposed for Zn/MnO<sub>2</sub> batteries, including Zn<sup>2+</sup> insertion/extraction,<sup>7,8</sup> Zn<sup>2+</sup> and H<sup>+</sup> co-insertion/extraction, 9,10 chemical conversion reaction mechanism,6 and the dissolution-deposition mechanism. 11,12 The first three mechanisms listed correspond to accessing the capacity from a one-electron redox reaction of Mn<sup>4+</sup>/Mn<sup>3+</sup>, exhibiting a rather limited capacity of 308 mA h g<sub>MnO2</sub><sup>-1</sup>. The dissolution-deposition mechanism has recently gained attention due to a higher theoretical capacity (616 mA h g<sub>MnO<sub>2</sub></sub><sup>-1</sup>) owing to the two-electron transfer reaction Mn<sup>4+</sup>/ Mn<sup>2+</sup>. <sup>13-15</sup> Wu et al. visualized and quantified the Mn dissolution-deposition process in the Zn/α-MnO<sub>2</sub> system via X-ray fluorescence microscopy which lays the foundation for understanding the dissolution-deposition chemistries. 11 The findings include the dissolution of Mn<sup>2+</sup> ions in the electrolyte and subsequent redeposition of solid manganese oxide and a nano-crystalline zinc-inserted layered chalcophanite phase (ZnMn<sub>3</sub>O<sub>7</sub>·3H<sub>2</sub>O). Kim et al. described the evolution of the complex phases formed in a tunneled α-MnO<sub>2</sub> exploring its mechanism by using transmission electron microscopy techniques. The study described the flower-shaped ZnMn<sub>3</sub>O<sub>7</sub>·3H<sub>2</sub>O in the electrode and a distorted ZnMn<sub>2</sub>O<sub>4</sub> on the α-MnO<sub>2</sub>. Tran et al. also discussed the formation of a flower-shaped complex which can attributed to the chalcophanite phase (ZnMn<sub>3</sub>O<sub>7</sub>· 3H<sub>2</sub>O) at 1.8 V formed in electrolytic manganese dioxide electrode.<sup>17</sup> Chen et al. proposed an amorphous phase to be forming during the charge state be a disordered layered Zn-Mn

oxide by operando Raman spectroscopy. 18 Hence, there is a need to investigate the capacity contributions of the different manganese oxide phases and further explore the reasons for battery degradation. Furthermore, if thoroughly understood, a controllable dissolution-deposition aqueous chemistry can become a viable strategy towards designing a range of versatile, environmentally friendly, and high-performance battery systems.

Operando characterization with synchrotron X-ray analysis is at the forefront of battery research owing to its tunable X-ray energy and high photon flux measurements that allow probing the batteries under real-time cycling conditions. 19 Synchrotron techniques thus have been significantly developed to study the working mechanisms of energy storage and conversion materials including the ones in battery science and technology. Fig. 1 illustrates the multimodal synchrotron techniques employed in our study, in which different complementary techniques were combined: operando X-ray absorption spectroscopy for characterizing the chemical state and short-range ordering, operando X-ray diffraction for providing the phase evolution and longrange structural changes, X-ray nano-tomography via transmission X-ray microscopy for visualizing the three-dimensional (3D) morphological evolution of the battery electrodes, and fluorescence microscopy for analyzing elemental and chemical changes. These techniques provide a holistic multimodal characterization approach that can be used to study complex issues involving morphological, chemical, and structural changes at various length scales in energy storage materials, as well as in other electrochemical systems. 19-23 The comprehensive information obtained from these techniques is crucial for understanding the underlying principles and mechanisms of battery operation and contributing towards developing new strategies for improving battery performance and sustainability in the

To this end, the goal of this work is to further understand the chemical, morphological and structural evolution happening in electrodes during the dissolution-deposition aqueous chemistry and evaluate the impacts of these changes on the battery performance. A Zn/β-MnO<sub>2</sub> battery system has been chosen, firstly for the benefits of the Zn aqueous batteries mentioned above. Additionally, amongst the different polymorphic structures of the  $MnO_2$ ,  $\beta$ - $MnO_2$  has a smaller  $1 \times 1$ tunnel structure in comparison with  $\alpha$ -MnO<sub>2</sub> having  $(2 \times 2)$  +  $(1 \times 1)$  tunnel structure and  $\gamma$ -MnO<sub>2</sub> with  $(1 \times 2) + (1 \times 1)$ tunnels and  $\delta$ -MnO<sub>2</sub> having a  $(1 \times \infty)$  layer polymorphs, making it challenging for Zn<sup>2+</sup> ions to intercalate. β-MnO<sub>2</sub> was thus chosen to study the potential dissolution-deposition reaction mechanism.<sup>24</sup> A multimodal approach was implemented to demonstrate the dissolution-deposition mechanism by emphasizing the various phases forming during the galvanostatic discharge and charge process. Operando X-ray diffraction and X-ray absorption spectroscopy were employed to study the phase evolution and local structure change, including quantitative modeling. In addition, X-ray microscopy via both transmission X-ray microscopy and μ-probe fluorescence microscopy was employed to study the three-dimensional (3D)

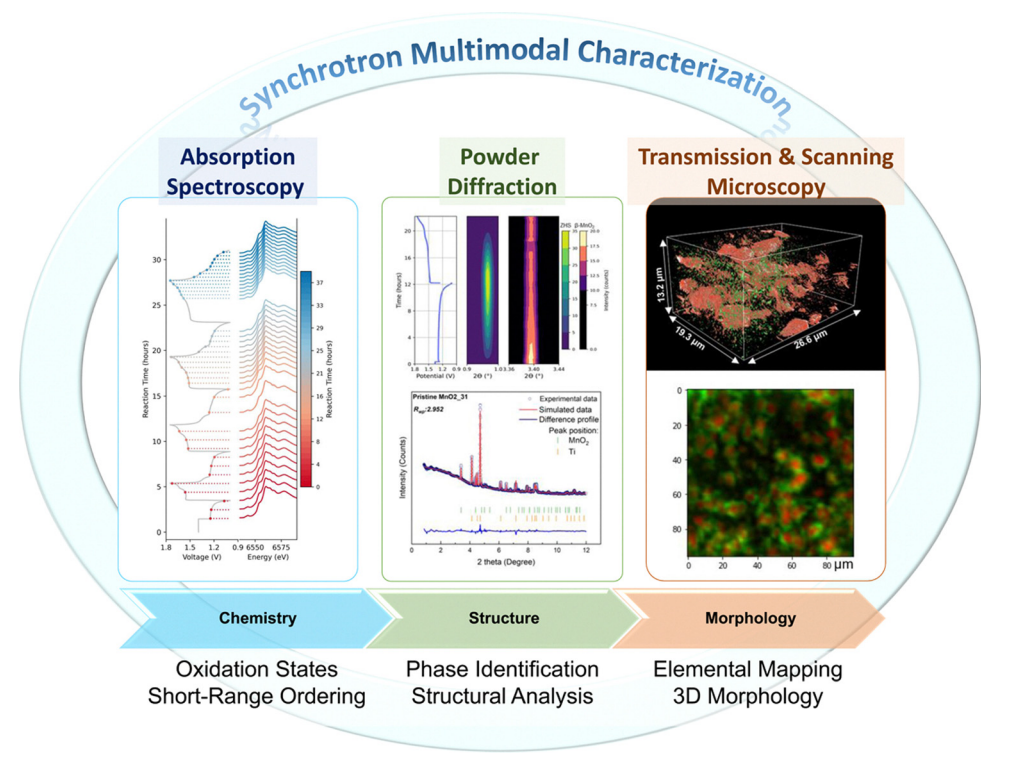


Fig. 1 Towards better understanding of reaction mechanism by operando multi-modal X-ray synchrotron characterization: the multimodal, operando synchrotron X-ray techniques implemented in the study with complementary modalities.

morphological evolution of the battery electrodes, coupled with the elemental and chemical changes. The various contrast and probing methods in multimodal synchrotron studies, combined with the operando studies can enable identification of the phase, local structure, and morphological evolution of the amorphous materials for Zn/MnO2 aqueous batteries in detail. Further understanding the formation and reversibility of complex redeposited phases and the overall evolution of the pristine electrode through multiple stages during battery cycling is essential to improving the capacity and cycle life. Overall, these analyses combined provides us a deeper understanding on the dissolution-deposition reaction chemistry which offers great potential for the future design of suitable electrode architecture for realization of scalable stationary energy storage.

### 2. Results and discussions

### 2.1 Dissolution of β-MnO<sub>2</sub> as the key capacity contributor

Operando synchrotron X-ray diffraction was conducted to study the crystalline phase evolution during the discharge and charge process for the first three cycles. 2 M ZnSO<sub>4</sub> with 0.1 M MnSO<sub>4</sub> electrolyte was used as the electrolyte and the β-MnO<sub>2</sub> electrode (Fig. S1, ESI†) was cycled under 1-1.75 V potential range at a constant current rate of 0.1C. The cell geometry and C-rate calculations are described in the Materials and methods section. MnSO<sub>4</sub> was added in the electrolyte as this enables the accessibility of Mn2+ ions at the electrode surface for adequate

rechargeability.<sup>25</sup> Fig. 2A shows the operando X-ray diffraction scans obtained at the pristine, end of the first discharge and the end of the first charge states. The two major phases in the cathode were identified from the diffraction data, including the original cathode material, β-MnO<sub>2</sub> (PDF-04-005-4365), and the newly formed reaction product, zinc hydroxy sulfate (ZHS) (PDF-04-012-8189). Titanium (PDF-04-006-2824) signals are also present, coming from the Ti foil used as the current collector.

Fig. 2B represents the electrochemical potential profile, and the operando diffraction results in a waterfall plot, plotted with respect to time. Two of the most prominent diffraction peaks are shown here, corresponding to the β-MnO<sub>2</sub> (110) and ZHS (001), respectively. The waterfall plot shows that there is a gradual formation of the ZHS phase for the discharge halfcycle followed by the disappearance of this peak during the charge half-cycle. During the discharge step, we observe a gradual reduction in peak intensity of β-MnO<sub>2</sub> without any change in the peak position (see Fig. 2B). The complete evolution of the XRD spectra is shown in the Fig. S2 (ESI†). In addition, two more peaks (101) and (211) of β-MnO<sub>2</sub> are plotted as water fall plots which are also uniformly decreasing during the discharge half cycle (see Fig. S3, ESI†). This indicates a onestep two-phase reduction reaction that can be attributed to the dissolution of  $\beta$ -MnO<sub>2</sub> as seen in eqn (1):

$$MnO_2 + 2H_2O + 2e^- \rightarrow Mn^{2+} + 4OH^-$$
 (1)

This dissolution of MnO2 leads to the increase in pH of the solution at the interface between the active materials of the

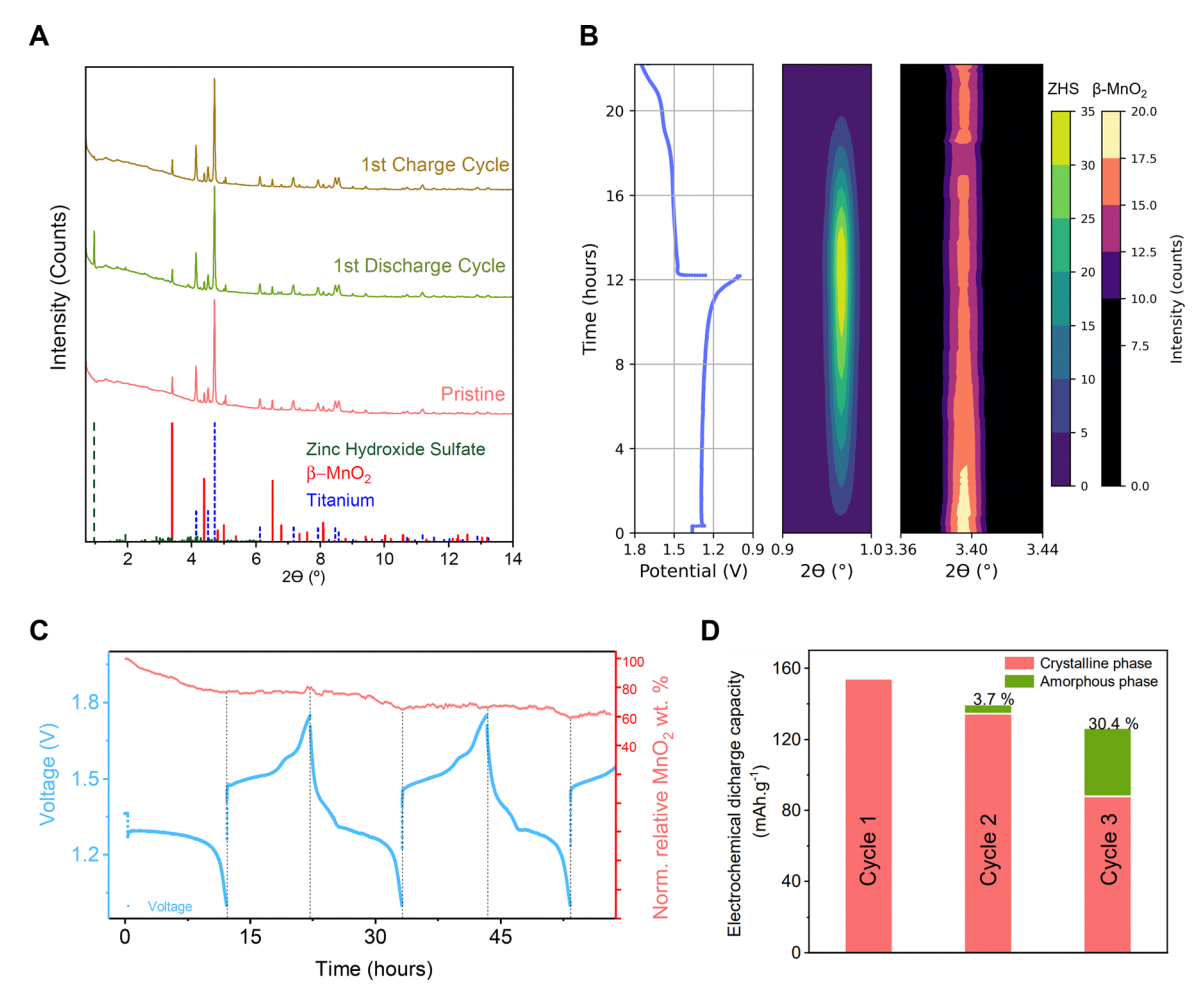


Fig. 2 (A) Operando X-ray diffraction results showing the phase evolution of the β-MnO<sub>2</sub> electrode at the pristine, half-cycle and full-cycle states. (B) The galvanostatic discharge-charge profile for the first cycle and its corresponding waterfall plot indicate the formation and disappearance of the ZHS phase and gradual reduction in MnO<sub>2</sub> peak intensity. (C) Normalized relative MnO<sub>2</sub> weight percentage plotted with respect to the electrochemical potential for the first 60 hours ( $\sim 3$  cycles). (D) Indicates the relative capacity contribution by the amorphous phase in the 2nd and 3rd cycles.

electrode and the electrolyte, leading to the precipitation of the ZHS phase, as shown in Fig. S4 (ESI†). The ZHS precipitates can be characterized as a dense plate-like morphology forming on the surface of the active material. This is indicative of a competing reaction between the  $MnO_2$  dissolution and ZHS deposition because of  $H^{\scriptscriptstyle +}$  consumption. This unique interplay between the manganese dissolution and zinc hydroxide precipitation should be kept in mind and will be further discussed in a later section.

To further elucidate this dissolution/deposition reaction mechanism quantitatively, three key parameters including the crystallite size, strain and the lattice parameters of the tetrahedral MnO $_2$  were calculated by Rietveld refinement of the *operando* XRD scans. Fig. S5A–C (ESI $^{\dagger}$ ) shows the Rietveld refinement fitting of X-ray diffraction spectra at three different representative states, namely pristine, fully discharged, and fully charged. The spectra were fitted for three components namely  $\beta$ -MnO $_2$  cathode, titanium current collector, and the ZHS precipitate. On obtaining good agreement with the observed and calculated patterns based on the weighted R-

factor value, the models were then used for further analysis of the full datasets for the X-ray diffraction. <sup>26</sup> Note that because ZHS is a complex triclinic phase, the corresponding diffraction pattern has many peaks, which may introduce uncertainty in the fitting process. The ZHS lattice parameters were thus fixed in the modelling while the analysis refines the other phases.

These crystallite size, strain and the lattice parameters were quantified based on the Williamson–Hall plot and provide an accurate measure of the extent of peak broadening and peak shift in the crystal lattice. Fig. S6 (ESI†) shows that negligible changes in the lattice parameters for both the a and c axes, as well as a microscopic strain value of <0.3%, supporting the lack of intercalation in the system. The relatively constant crystallite size during the discharge and charge process can be explained by the preferential dissolution of the smaller MnO<sub>2</sub> crystals, and thus the overall averaged crystallite size was a result of the balance between the dissolution mechanism and the disappearing of small crystals.

During the charge step, increase in the MnO<sub>2</sub> peak intensity was not visible neither was the formation of any new peaks,

indicating that the redeposition phase may be amorphous. To relate the manganese dissolution to the overall capacity of the battery, the weight fraction of β-MnO2 was also evaluated by Rietveld refinement of the operando diffraction data. The fitted β-MnO<sub>2</sub> weight percentage is normalized to the weight percentage of the titanium current collector since the amount of titanium in the X-ray beam remains constant and can serve as a reference to account for the beam intensity fluctuation. As visualized in Fig. 2C, in the first discharge cycle, the normalized weight percentage reduces by 25 wt%. which corresponds to 154 mA h g<sup>-1</sup> of capacity (considering a theoretical capacity of 616 mA h g<sup>-1</sup>). As observed in the electrochemical data in Fig. 2B, the discharge capacity corresponds to  $\sim 150$  mA h g<sup>-1</sup>. Thus, the dissolution of β-MnO<sub>2</sub> is the primary contributor to the electrochemical capacity of the battery. In the second and third cycle a similar trend could be observed where dissolution of MnO<sub>2</sub> occurs in the discharge half cycle and no formation of new peaks visible. Another important trend that can be observed for the second and third cycle is that the electrochemical capacity retention is higher than the remainder of the crystalline MnO<sub>2</sub> phase (see Fig. 2D and Table S2, ESI†). It is thus possible that an amorphous phase formation can account for the difference in capacity. The difference between the total electrochemical capacity quantified from the electrochemical data and crystalline phase capacity obtained from Rietveld refinement could be due to the formation of an amorphous phase, and thus contribute to the overall capacity. In particular, during the 3rd cycle, a significant capacity contribution of  $\sim$  40 mA h g $^{-1}$  can be attributed to the amorphous phase. This contribution from the amorphous phase may continue increasing in the subsequent cycles, which will be discussed in the subsequent analysis. Li et al. reported that rate limiting and irreversible conversion reactions occur in in situ deposited MnO<sub>2</sub> batteries employing 1 M ZnSO<sub>4</sub> + 0.2 M MnSO<sub>4</sub> at a cell voltage lower than 1.26 V, hence cycling between 1.3-1.8 V improved power and rate capability.<sup>28</sup> The active material dissolution and the formation of ZnMn<sub>3</sub>O<sub>7</sub>·xH<sub>2</sub>O was attributed to be the reason for irreversibility. To further investigate the irreversible reactions, operando X-ray diffraction was used to measure the cells between a reduced voltage range of 1.3-1.75 V after an initial activation cycle between 1-1.75 V. As seen in Fig. S7 (ESI†), when cycling between the 1.3-1.75 V voltage range, there was an absence of the ZHS peak in the diffraction scans. This infers that ZHS formation during the discharge half-cycle may also be related to the irreversibility of the electrode over longer cycles. The formation of ZHS is a result of consumption of protons from the dissolution of  $MnO_2^{14}$  and thus the absence of the ZHS formation indicates that there is no dissolution of MnO2 taking place in the reduced voltage range (1.3-1.75 V). Hence, the capacity contribution in this reduced voltage range may be a result of the reversibility of the amorphous phase that may have formed at the end of the first activation cycle.

In addition, as observed in Fig. S8 (ESI†) the relative ZHS weight is plotted with respect to the electrochemical potential for the same *operando* diffraction studies as shown in Fig. 2.

In charge and discharge potential range  $\sim 1.3$ –1.75 V, as indicated by the orange boxes, there is negligible change in the ZHS weight, indicating the absence of redeposition and dissolution of the MnO<sub>2</sub> electrode. Hence, as observed in Fig. 2C, the gradual decrease in the relative MnO<sub>2</sub> weight percentage in the subsequent second and third cycles was the most prominent during the second discharge plateau after 1.3 V. This indicates that the plateau between 1.75–1.3 V can be attributed to the reversible dissolution of the amorphous phase formed during the charge steps in the first and second cycles. The electrochemical reaction for the amorphous phase region is discussed in the proposed reaction mechanism and reasons for rise in pH section of the results and discussions.

### 2.2 Gradual transition from crystalline to amorphous phase

Operando X-ray diffraction was able to capture the evolution of the crystalline phases, including the time-dependent dissolution of  $\beta$ -MnO<sub>2</sub> and the formation of the ZHS phase. The absence of crystalline phase formation during the charge stage indicates the reaction products are not crystalline, but an amorphous phase. To provide more information on this amorphous redeposition phase and to better understand the transition from the pristine crystalline  $\beta$ -MnO<sub>2</sub> to the amorphous phase, synchrotron operando and ex situ X-ray absorption spectroscopy (XAS) were performed across the Mn and Zn K-edges to determine the chemical states and the local structural changes of the Mn and Zn containing phases during the reactions.

Operando XAS studies were carried out in a pouch cell configuration which enables scanning a larger area to mitigate any potential beam damage.29 More information regarding the operando experiment setup is described in the Materials and methods section. In the pouch cell configuration, the electrolyte and β-MnO<sub>2</sub> coated on titanium is present in the beam path, hence the XAS spectra collected during the operando scans are the combination of the two spectral components. Fig. 3A shows the operando X-ray absorption near-edge structure (XANES) spectra across the Mn K-edge as a function of the electrochemical potential for the first 5 cycles. The aqueous Zn/β-MnO<sub>2</sub> battery was cycled at a C-rate of 0.2C. As indicated with a black line passing through the white lines (in Fig. 3A) position of the spectra, there is no detectable edge shift but there is a slight shift of the spectra towards the left as observed by the selected spectra at the end of each discharge and charge potentials (represented by decreasing intensity a red and violet color scales) shown in Fig. 3B. This indicates that the overall structure after the discharge and charge process is evolving towards a reduced state. In addition, changes in pre-edge feature were also evidently observed, as indicated by a red arrow (for charged states) and a blue arrow (for the discharged states) showing the direction of change in the pre-edge factor for increasing number of cycles, indicating the chemical composition is changing in the Mn-containing phases, despite having the same white line energy. As the cell is reaching the discharge state, the intensity of the pre-edge feature increases in comparison to the pristine electrode. This can be explained

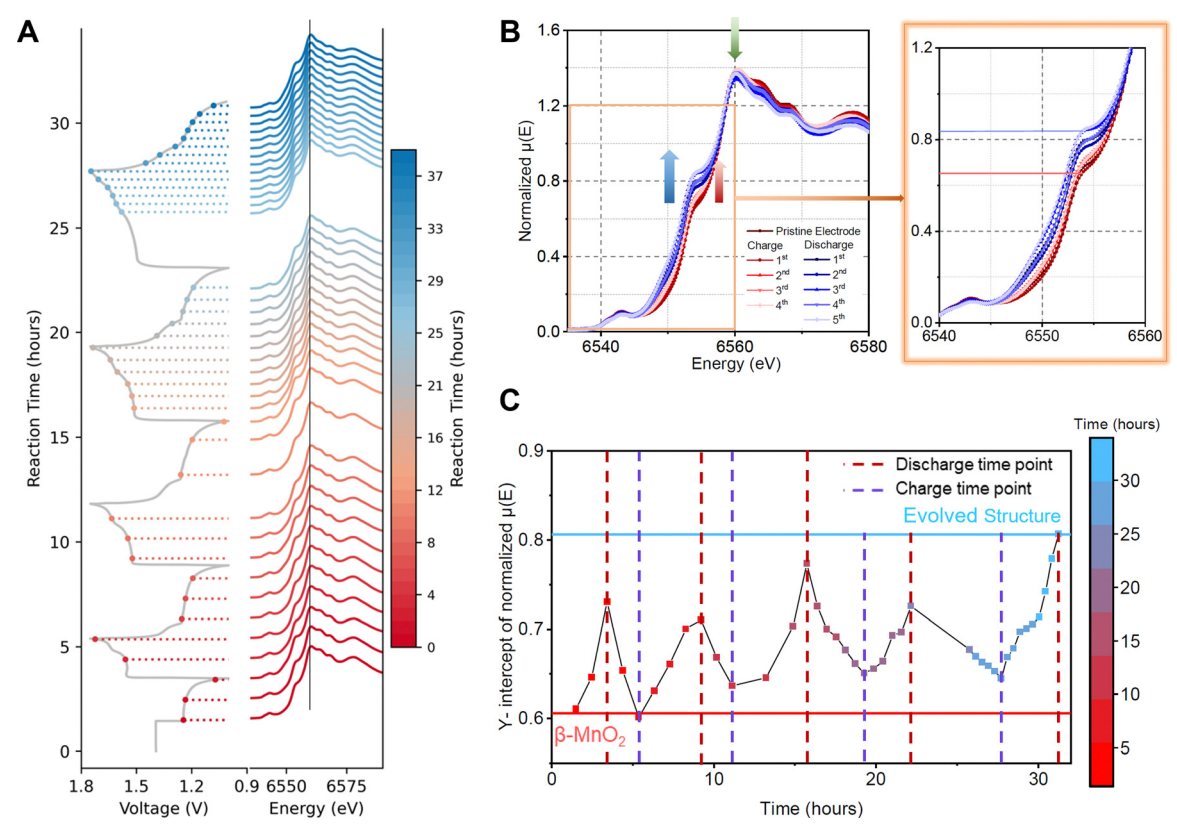


Fig. 3 Operando XAS results across the Mn K-edge indicating the gradual conversion of  $\beta$ -MnO<sub>2</sub> structure in 2 M ZnSO<sub>4</sub> + 0.1 M MnSO<sub>4</sub> electrolyte. (A) Operando XANES spectra plotted with respect to the electrochemical potential and reaction time. (B) Selected spectra points taken at the end of discharge and charge profiles of the operando XAS. The inset plot shows the variation in the pre-edge feature.  $\mu(E)$  refers to the X-ray absorption coefficient (a.u.). (C) Y-intercept of normalized XAS spectra near the pre-edge feature indicating the evolution of structure.

by the increase in Mn(II) species in electrolyte because of the dissolution of MnO<sub>2</sub> (see Fig. S9, ESI†).

As the Mn(II) in the liquid phase is a reduced species, this causes a positive shift in the pre-edge feature towards the lowerenergy direction indicated in Fig. 3B and in the inset plot. This is in line with the results that were obtained in operando fluorescence microscopy imaging by Wu et al. 11 During the charge state a reverse trend is observed: the pre-edge feature returns to the pristine state in the first cycle and then gradually drifts to a reduced charge state. This indicates that there is a gradual formation of a Mn-containing compound with a more reduced chemical state during the charge state as viewed in the lighter shade of red in Fig. 3B. This reduced Mn-containing compound identified here in the operando XAS analysis likely corresponds to growth of an amorphous phase during the electrochemical cycling, inferred by the operando XRD analysis. To better understand this growth of amorphous phase, the yintercept of the normalized spectra is plotted for at an energy around the maximum variation in the pre-edge feature, as shown in Fig. 3C. The range of the y-intercept in represented by the red and violet lines in Fig. 3B inset graph. As the operando cell discharges and charges the y-intercept increases and decreases. As the dissolution increases from the activation cycle the y-intercept further increases; but during charge the y-intercept does not return to its original position. This can be

attributed to the reduced deposited phase which is expressed as the evolved new Mn-Zn complex phase in Fig. 3C.

### 2.3 X-ray absorption spectroscopy to analyze the formation of a new phase

During the discharge, dissolution of Mn(IV) to Mn(II) in the initial cycles was found to be the key capacity contributors in the initial cycles of aqueous Zn/β-MnO<sub>2</sub> battery. From *operando* spectroscopy, a gradual formation of a reduced state is visible during the charge state and this state increases with increasing cycle number. To negate the effect of Mn(II) ions from the electrolyte and to observe the oxidation state of the bare electrode, ex situ samples were prepared and analyzed at different cycling conditions. The pristine (as-prepared) electrode, first cycle and eight cycle ex situ samples were analyzed with XAS at both Mn and Zn absorption edges. Detailed procedure for the preparation of the ex situ samples is explained in the Materials and methods section. Contrary to the operando XAS measurements, the first cycle discharge spectra (see Fig. 4A) collected at the Mn K-edge resembles the pristine spectra. This indicates that there is no new phase forming during discharge and supports the claim that the Mn(II) dissolution (from solid to liquid phase) is the primary contributor to capacity as demonstrated by the eqn (1).

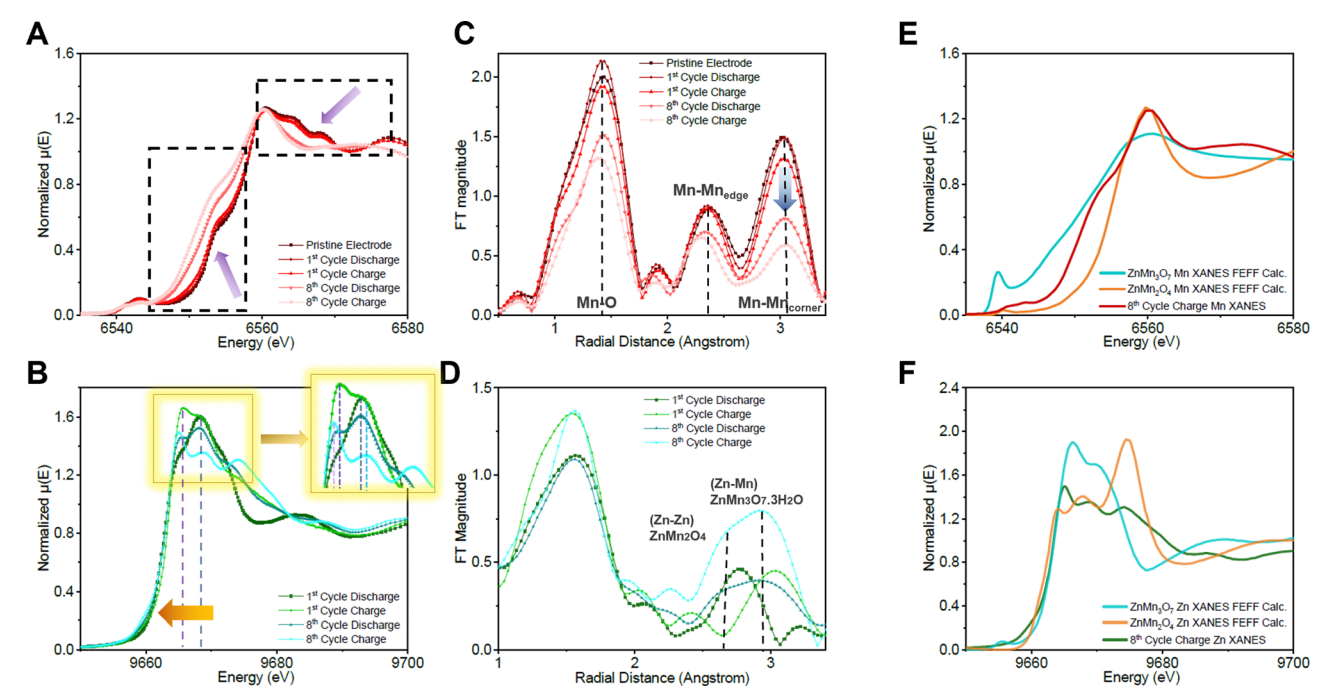


Fig. 4 (A) Mn and (B) Zn K-edge  $ex\ situ\ XAS$  of first and eight cycle discharge (at 1.0 V) and charge (at 1.75 V) of  $\beta$ -MnO<sub>2</sub> electrodes. (C and D) EXAFS analysis showing the R-space spectra of the first and eighth cycle samples at the corresponding discharge and charge state. (E and F) Correspond to the comparison between the eight-cycle charge sample across the Mn and Zn K-edge with the ZnMn<sub>2</sub>O<sub>4</sub> and ZnMn<sub>3</sub>O<sub>7</sub> FEFF calculated spectra.

For the first cycle charge state as observed in the *ex situ* XANES (in Fig. 4A) there is a gradual shift in the direction indicated by the red arrow suggesting a reduced state in comparison to the pristine state. After eight cycles in Fig. 4A, distinct changes in the pre- and post-edge features indicated by purple arrows are visible in comparison to the spectrum from the pristine state, indicating that the transformation of the  $\beta$ -MnO $_2$  electrode into another phase. Based on the EXAFS data collected at the Mn K-edge, the *R*-space analysis for the first and eight cycled samples as seen in Fig. 4C showed that the Mn–Mn bond for the corner atoms significantly decreases (as indicated by the blue arrow) for the eight-cycle charge sample, indicating a structural change in the compound. This indicates that deposited phase may not have the corner-shared octahedra.

With the possibility of having zinc in the manganese complex phases as a result of the presence of Zn<sup>2+</sup> ions from the electrolyte, XAS was measured across the Zn K-edge for both the 1st and 8th cycle data as shown Fig. 4B. The Zn XANES spectrum of 1st cycle discharge sample has a single white line peak (indicated by a dark blue dashed line in Fig. 4B); this is consistent with the X-ray diffraction data presented in the prior section, showing that ZHS was formed during discharge half cycle. The same white line position is also present in the Zn XANES spectrum of the 8th cycle discharge sample, consistent with the formation of ZHS upon the discharge of the battery. Upon charging, this white line position shifts slightly towards the higher energy (indicated by a lighter blue dashed line in the inset of Fig. 4B). Considering the disappearance of the ZHS phase during charging as shown in the XRD analysis, this white line shift likely corresponds to the formation of one of the

Zn-Mn complex phases. Additionally, another more prominent white line feature appeared at the lower energy in the Zn XANES spectrum of the 1st cycle charge sample (indicated by a dark purple dashed line in Fig. 4B; an orange arrow indicates this large energy difference between the two white-line positions). This shows that there is at least another Mn-Zn complex phase, with a different structure, present in the charged state of the cathode material. Upon more cycling, this lower energy white line position further shifted towards a lower energy as shown in spectrum of the 8th cycle charge (indicated by a lighter purple dashed line in the inset of Fig. 4B), indicating that this complex phase(s) continue to evolve upon cycling; its changing in the relative intensity between charge and discharge states may also indicate that it is at least partially reversible. This phase is similar to the layered Zn-birnessite (ZnMn<sub>3</sub>O<sub>7</sub>·2H<sub>2</sub>O). This complex phase has been previously reported and observed under nano-characterization techniques such as STEM imaging and TEM diffraction. 14,16,30 In addition, the 8th cycle charge XANES resembles the ZnMn<sub>2</sub>O<sub>4</sub> (hetaerolite) phase.<sup>31</sup> Based on the EXAFS data collected at the Zn K-edge (see Fig. 4D), the R-space analysis shows that the 8th cycle charge and discharge samples are similar. The 8th cycle charge has a higher FT magnitude than the first cycle spectra indicating that the deposited phase may have increased in concentration with higher cycles. Also, the decreasing intensity of the Mn-Mn<sub>corner</sub> raises the question if this may be due to the growth of a Zn-Mn coordination. For the eight-cycle charge and discharge spectra a characteristic peak at 1.5 Å and a broad peak between 2.5 to 3.4 Å. On comparing these with the FEFF calculated paths we observe that the broad peak may be the result of two

components namely the ZnMn<sub>3</sub>O<sub>7</sub>·2H<sub>2</sub>O which has a FT magnitude of Zn-Zn coordination at ~3.2 Å and ZnMn<sub>2</sub>O<sub>4</sub> has Zn-Mn coordination at  $\sim 1.4$  and 2.7 Å as seen in Fig. S10 (ESI<sup>†</sup>).

To further study the contributions from the two complexes ZnMn<sub>3</sub>O<sub>7</sub>·2H<sub>2</sub>O and ZnMn<sub>2</sub>O<sub>4</sub>, the XAS spectra is calculated and compared with the 8th cycle charge sample. The XAS spectra is calculated by the FEFF program which is a multiple-scattering ab initio code for computing excitation spectra and electronic structure for a cluster of atoms generated from the crystallographic file. 32,33 The input for the FEFF calculations were generated by the standard crystallographic information files for ZnMn<sub>3</sub>O<sub>7</sub>·2H<sub>2</sub>O (PDF #04-011-5216) and ZnMn<sub>2</sub>O<sub>4</sub> (PDF #04-002-4954). More information regarding the parameters used for the analysis is described in the Materials and methods section. The calculated spectra are presented for X-ray absorption across the Mn K-edge (see Fig. 4E) and Zn Kedge (see Fig. 4F). Based on the calculated spectra 8th cycle charge spectra across the Mn-K edge seems to be a combination of both ZnMn<sub>3</sub>O<sub>7</sub>·2H<sub>2</sub>O and ZnMn<sub>2</sub>O<sub>4</sub> (represented by the dashed lines).

More evident proof for this can be found in the data across the Zn K-edge. The peak at the lower energy has the highest intensity for the ZnMn<sub>3</sub>O<sub>7</sub>·2H<sub>2</sub>O in addition to another peak at a lower energy whereas ZnMn<sub>2</sub>O<sub>4</sub> has three peaks with the highest intensity peak at the higher energy. The XAS for the 8th cycle charge sample across the Zn K-edge seems to be a combination of both the complexes having the highest intensity for the first peak at lower energy. The presence of the other two peaks indicates that there exists a contribution from the ZnMn<sub>2</sub>O<sub>4</sub> spectra. Further XAS data analysis including decomposition of operando spectra into pure components and their respective concentrations is discussed with multivariate curve resolution (MCR) method in the later section.

### 2.4 Key morphological features of β-MnO<sub>2</sub> electrodes

Synchrotron X-ray nano-tomography was conducted at the fullfield X-ray imaging (FXI) beamline at the National Synchrotron Light Source (NSLS-II) to visualize the morphological evolution of the electrode, corresponding to the phase and chemical changes, at different cycles and at the end of discharge (1.0 V) and charge (1.75 V) electrochemical potentials. The procedure for obtaining a 3D volume rendering is described in the Materials and methods section. Fig. 5 presents the morphological evolution as observed in a 3D volume rendering view, and two orthogonal pseudo-cross-sectional views for pristine, first and sixteenth cycle discharge and charge and eight cycle charge electrodes, above Mn, and Zn K energy absorption edges. The comparison between the two energies is done to contrast and compare the morphologies of the Mn- and Zn-containing phases. Hence, by subtracting the below-edge image from above-edge for the specific element, Zn and Mn phases forming during the electrochemical reaction can be better identified.<sup>34,35</sup>

For the pristine electrodes, the micron size β-MnO<sub>2</sub> particles can be visualized from the images collected above the Mn edge (see Fig. 5A). Since the carbon additive is almost transparent to X-ray at the Mn and Zn absorption edges, they have a low

contrast and are invisible in the 3D views. During the first discharge, a dense growth of ZHS precipitate is visible on the electrode, as indicated by the white arrows in Fig. 5B. This growth of the ZHS phase leads to features corresponding to a flake-like nanosheets; the same structure when viewed orthogonally look like needle like precipitates. In addition, as seen in the subtracted views across the Zn edge, these phases seem to be primarily rich in the Zn. Also, on comparing the subtracted views across the Mn and Zn edge colocalization of the Zn phase and Mn phases is not visible. This indicates that there may be absence of Zn intercalation or formation of a conversion product with the β-MnO<sub>2</sub> cathode material during discharge. Another key feature to observe here is that the ZHS appears to be forming at the location of manganese dissolution as indicated with a dotted box in Fig. 5B. During the first discharge, only  $\sim 25\%$  of the  $\beta$ -MnO<sub>2</sub> appears to be dissolving as observed from the operando diffraction studies. One of the probable reasons for this limited dissolution of β-MnO<sub>2</sub> can be attributed to the dense ZHS growth over the active material. 13 The benefit of this growth could be that the ZHS phase may be able to trap the Mn(II) ions formed from the dissolution to  $\beta$ -MnO<sub>2</sub>, thereby improving the reversibility during the charge half cycle.

To further understand this real time colocalization of the Zn and Mn phase around the electrode, operando X-ray fluorescence imaging was carried out at the Submicron Resolution X-ray spectroscopy (SRX) beamline at NSLS-II. Operando fluorescence map taken at the end of third discharge cycle is represented in Fig. 6A. From the overlapping and corresponding Zn, Mn maps (indicated by the red box) the coexistence of Zn and Mn phases is visible which can be attributed to the liquid phase Mn(II) and the ZHS precipitate. In the subsequent charge cycle as seen in Fig. 5C, the ZHS phase is not visible, indicating that the ZHS phase is reversible. Reversibility of the ZHS phase is also visible from the diffraction studies shown in Fig. 2B. In the charge state, the MnO<sub>2</sub> particles are visible whereas the Zn-Mn complex phase is not. This observation can be attributed to the less prevalence of Zn-Mn complex phase due to the minimal X-ray absorption when compared to the MnO<sub>2</sub> particles.

The corresponding fluorescence map captured at the end of the 3rd cycle charge state confirms that the Zn phase is distributed throughout the electrode (see Fig. 6B). In the 8th cycle charge state, two distinct morphologies are visible, comprising of MnO<sub>2</sub> particles (white box) and Zn-Mn complex (dotted white box) in Fig. 5D. This can also be characterized by the difference in X-ray attenuation, where the brighter phases are MnO2 particles and the low contrast phases are Zn-Mn complex. Also in this figure, the dissolution of MnO<sub>2</sub> particles results in voids in the electrode (in red box). At certain locations the Zn-Mn complex seems to be depositing in the proximity of MnO2 dissolution. This can be visualized in Fig. 5D in the region with the dotted red box. Fig. 5E and F, represent the 16th cycle discharge and charge phases respectively. The number of voids is significantly higher due to the increase in dissolution of the MnO2 particles (Fig. 5E dotted dark blue box). These voids cause a break in electronic

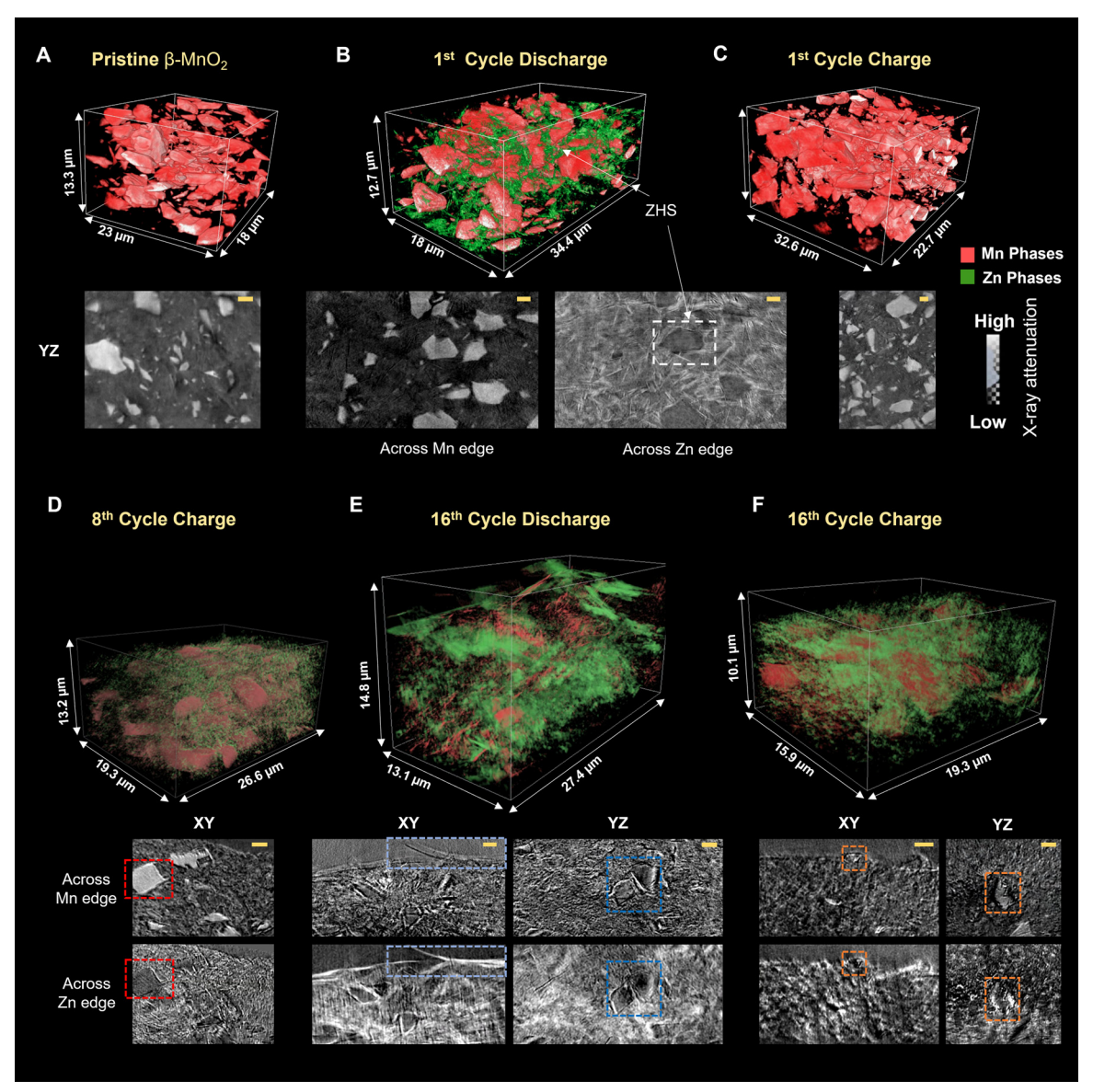


Fig. 5 3D synchrotron X-ray nano-tomography by transmission X-ray microscopy for visualizing the morphological evolution of the β-MnO<sub>2</sub> electrodes as a function of electrochemical cycling. (A) Pristine, (B) first discharge state (at 1.0 V), (C) first charge state (at 1.75 V), (D) the 8th cycle charge state which can be characterized by the partial dissolution of  $\beta$ -MnO $_2$  particles and the Zn-Mn amorphous complex phase. (E and F) Represents the 16th cycle discharge and charge state characterized by dissolution of β-MnO<sub>2</sub> and dense growth of Zn phases throughout in the electrode. The ROI boxes of a specific color are of the same sizes and are at the same locations for the cross sections across Mn and Zn K-edge. The scale bar represents 2 µm.

pathways of the electrode as this may lead to a loss in contact with the carbon additive. The dense growth of the ZHS precipitate is visible throughout the electrode (Fig. 5E dotted light blue box). In addition, the presence of dispersed morphology of the Zn-Mn complex indicates the irreversibility of this phase. In Fig. 5F, the distinct plate-like morphology of the ZHS phase is completely absent; however, a dispersed phase containing the Zn-Mn complex is observed throughout the electrode. As observed in the dotted orange box the redeposited phase seems to be forming a shell-like structure around the  $MnO_2$  particles. This indicates that the deposition may not be occurring in the void formed due the MnO2 dissolution but on the plate-like

morphology of the ZHS precipitate which forms as an immediate result of the dissolution. To examine this mechanism, cathode without MnO2 active material was prepared following the same experimental conditions as the preparation of a coin cell (elaborated in Materials and methods section). Fig. S11 (ESI†) depicts the nucleation of the Zn-Mn complex over carbon black. For the second cycle the nucleation overpotential was reduced by 27 mV indicating the improvement of nucleation of the Zn-Mn complex phase. This may be due to the deposition of the Zn-Mn complex phase over the ZHS precipitate which is formed in the previous discharge half cycle.

### 2.5 Phase evolution after extended cycles leading to cell degradation

As presented in the prior sections, the results show that the dissolution of MnO<sub>2</sub> particles was followed by the subsequent deposition of a low crystallinity Zn-Mn complex. This behavior was further analyzed in aqueous Zn/β-MnO<sub>2</sub> batteries after more extended cycling at a lower C rate (0.1-0.2C) to understand the reaction mechanism. This lower C rate was helpful for the investigation as the capacitive contribution of the batteries is negligible when compared to the high C rate data which is superior in terms of cycle life and rate capability. 4 The electrochemical data were shown in Fig. S12 (ESI†). The first 100 hours of cycling (~10 cycles), two discharge and charge plateaus are visible. After 300 hours of cycling (18 cycles), the plateaus are no longer present in the cycling profiles. This can be attributed to the continuous amorphization of the electrode. The continuous dissolution of particles creates voids, and the deposition of the amorphous phase occurs over the surface of β-MnO<sub>2</sub> particles. This leads to the loss of integrity and electronic pathways throughout the electrode. Fig. 6C shows the surface characterization of the 1st cycle surface charged sample by SEM. A dense flower-like particle is formed over the MnO<sub>2</sub> particles which seem to be crystalizing over the electrode surface as indicated in the dotted red box. The charged sample shows a smoother deposition throughout the surface in comparison to the pristine MnO<sub>2</sub>. The ex situ synchrotron X-ray diffraction study of MnO2 electrode at the 8th and 32nd cycle, in a charge state, is depicted in Fig. 6D. The laboratory XRD spectra comparing the 8th, 16th and 32nd charge electrodes are presented in Fig. S10 (ESI†). A new ZnMn<sub>2</sub>O<sub>4</sub> (hetaerolite) phase with broad peaks is visible at 4.31°, 3.95° and 3.50° corresponding to the (2 1 1), (1 0 3) and (1 1 2) planes. The crystal structure and the different views are presented in Fig. S13 (ESI†). The intensity of the ZnMn<sub>2</sub>O<sub>4</sub> phase is higher in the 32nd cycle charge sample indicating that this phase may be

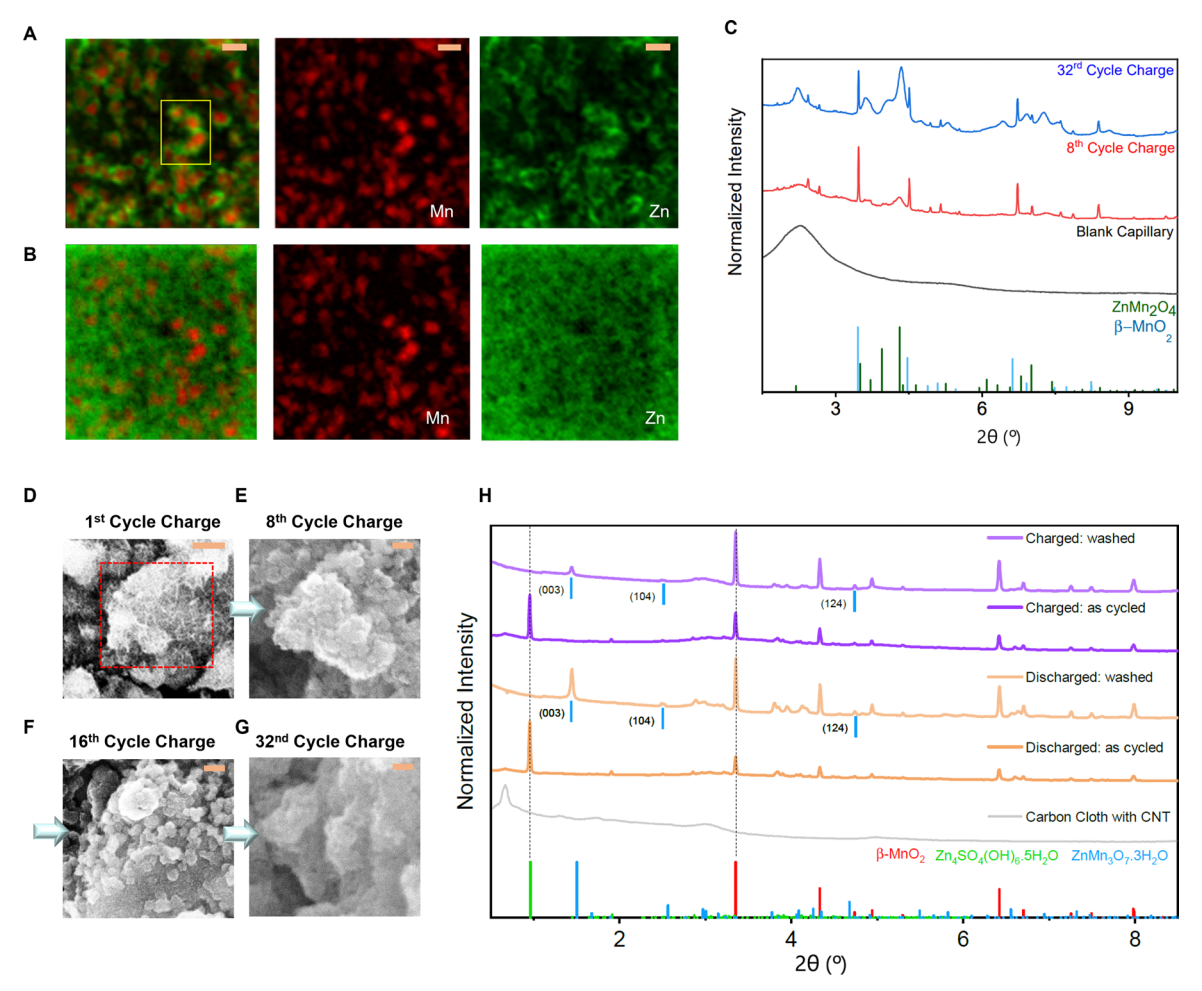


Fig. 6 Operando XRF maps, X-ray diffraction, surface characterization to study reason for capacity fade and operando drying experiment. Overlay and individual operando fluorescence microscopy maps from the third cycle: (A) discharged (1.0 V) and (B) charged (1.75 V) states of the β-MnO<sub>2</sub> electrode. The yellow box in (A) indicates the colocalization of the Zn phase over the  $MnO_2$  particles. The scale bar in the individual maps indicates 5  $\mu$ m. (C) X-ray  $diffraction\ spectra\ showing\ the\ growth\ of\ the\ hetaerolite\ (ZnMn_2O_4)\ phase\ obtained\ at\ the\ end\ of\ eight\ and\ thirty\ second\ cycle.\ (D)\ FSEM\ of\ first\ cycle$ ex situ sample at the charged state having a flower like deposition over the MnO<sub>2</sub> particle. FSEM results of the (E) eight, (F) sixteenth and (G) thirty second cycle showing the growth of spherical round feature, scale bar, 500 nm D, 100 nm (E-G), respectively. (H) X-ray diffraction measurement of the electrode at discharge and charge state as cycled and after washing.

irreversible and hence the concentration may be increasing with cycles. Another feature of the  $ZnMn_2O_4$  spectra is the peak broadening, indicating the deposited phase may be nano particles, small grains, or grains with lower crystallinity. The  $ZnMn_2O_4$  phase is a thermodynamically stable phase which experiences strong electrostatic repulsions of the  $Zn^{2+}$  ions, making their insertion into this lattice complicated.<sup>37</sup>

The mechanism for irreversibility of the ZnMn<sub>2</sub>O<sub>4</sub> phase is explained below. The dissolution of MnO<sub>2</sub> active material as a result of proton consumption during the discharge is described as shown in eqn (1). This leads to the increase in the local OH<sup>-</sup> concentration which is neutralized by the formation of ZHS precipitate. The accumulation of ZHS precipitate over the subsequent cycles leading to an increase in pH of the battery. This increase in pH has been reported in the literature.<sup>36</sup> Another recent study has reported that the pH of the electrolyte in aqueous Zn-MnO<sub>2</sub> batteries evolves spontaneously towards a higher pH due to reaction between Zn metal and protons present in the electrolyte.<sup>38</sup> The phase formation of this complex might be as described in the eqn (2). Fig. 6E-G shows the gradual growth of the ZnMn<sub>2</sub>O<sub>4</sub> nanoparticle phase in the 8th, 16th and 32nd cycles respectively. As seen in the surface characterization in the SEM images, spherical ZnMn<sub>2</sub>O<sub>4</sub> seems to be forming and eventually leading to a mossy like morphology over the MnO2 particles. This unreactive phase formation over the surface of the electrode causes capacity to fade as seen in Fig. S14 (ESI†) leading to the eventual failure of the battery.

$$Zn_{(aq)}^{2+} + Mn_{(aq)}^{2+} + MnO_{2(s)} + 2H_2O \rightarrow ZnMn_2O_{4(s)} + 4H^+$$
(2)

Based on this reaction mechanism, this battery chemistry can continue to function even after the MnO<sub>2</sub> active material has been fully consumed over extended cycles. When the MnO<sub>2</sub> dissolves during discharge, the growth of a dense layer of ZHS may create a diffusion barrier that limits further dissolution of the active material. During the charge step, an amorphous Zn–Mn containing charge product may be depositing on the surface of ZHS precipitate which forms over the MnO<sub>2</sub> particles. Therefore, the battery's life is not limited by the MnO<sub>2</sub> present in the system but by the extent to which this reversible amorphous Zn–Mn phase can continue to cycle without the forming the irreversible complex phases due to a rise in the pH of the battery.

# 2.6 *Operando* drying experiment at different electrochemical states

The absence of X-ray diffraction peaks during the charge half cycle of the poorly crystalline  $ZnMn_3O_7\cdot 3H_2O$  (chalcophanite) phase raises questions regarding the nature of this phase. Even though this phase has been reported by advanced characterization such as STEM imaging and TEM diffraction, *operando* analysis of this phase has not yet been reported. Hence, a unique *operando* synchrotron X-ray diffraction experiment was designed to investigate this phase. The same  $\beta\text{-MnO}_2$  material was vacuum infiltrated onto an activated carbon felt with CNT additive. This strategy was implemented to improve the areal loadings of the

electrode along with minimization of the background caused by the titanium current collector caused in the diffraction pattern as a result of the X-ray measurement in the transmission mode. 1 M  $\rm ZnSO_4$  without 0.1 M  $\rm MnSO_4$  was used as the electrolyte since the  $\rm Mn^{2+}$  from the  $\rm MnSO_4$  may contribute towards the capacity of the battery. The cell configuration and the setup are described in the Materials and methods section.

Two operando cells with Kapton windows were cycled to the electrochemical discharge and charge states respectively. Prior to disassembly of the battery cells, both at the discharge and charge state show the presence of two phases, β-MnO<sub>2</sub> and ZHS phase (Fig. 6H, darker orange, and purple curves). The presence of ZHS in the charge state can be explained by the low coulombic efficiency because of the absence of MnSO<sub>4</sub> additive in the electrolyte. After measuring the diffraction spectra, the cells were immediately disassembled and washed with high purity water and remeasured during the drying process. The time taken for disassembly and washing was  $\sim$ 75 min. These diffraction scans (Fig. 6H, lighter orange, and purple curves) indicate the presence of the ZnMn<sub>3</sub>O<sub>7</sub>·3H<sub>2</sub>O phase (PDF-04-012-1275) along with the  $\beta$ -MnO<sub>2</sub> phase. The diffraction peaks (003), (104) and (124) of the ZnMn<sub>3</sub>O<sub>7</sub>·3H<sub>2</sub>O phase are visible. Interestingly the intensity of the ZnMn<sub>3</sub>O<sub>7</sub>·3H<sub>2</sub>O in the discharge state is more prominent than in the charge state indicating that this phase may have formed as a result of recrystallization of the Mn ions resulting from the electrode dissolution. A similar observation of the chalcophanite phase during the discharge state of α-MnO<sub>2</sub> has been claimed by Lee et al.<sup>8</sup> On vacuum drying the electrode at 60 °C for 6 hours the electrode continues to show the presence of chalcophanite phase (see Fig. S15, ESI†). Based on these studies we can conclude that this ZnMn<sub>3</sub>O<sub>7</sub>·3H<sub>2</sub>O phase, which has been previously perceived to be the direct reaction product in the charge state, is indeed a derived phase from unreacted Mn-ions present in the electrode. This hence illustrates the significance of the primary reaction product, which is indeed a disordered/amorphous Zn-Mn complex phase that has not been identified previously.

### 2.7 Phase evolution studied by the MCR-ALS analysis

To further resolve the evolution of the Mn–Zn complex phases, here a multivariate curve resolution (MCR) analysis was implemented on the *operando* XAS dataset across the Mn and Zn absorption K-edges. MCR is a suite of techniques used to decompose spectral datasets into the spectra of pure components and their respective abundances or concentrations. Alternating least squares (ALS) is becoming a popular MCR technique due to its robustness and relative simplicity in implementation.<sup>39</sup> MCR-ALS begins with an initial guess of the pure component spectra or concentration profiles and then iteratively applies least squares regression to repeatedly fit the spectra and concentrations until a convergence criterion is met. Implementation of this technique is further elaborated in the Materials and methods section.

The XANES Mn K-edge data from the  $MnO_2$  operando experimental dataset discussed in Fig. 3 was employed to breakdown the different components of the spectra. Based on

the principal component analysis by singular value decomposition of the dataset see Fig. S16 and S17 (ESI†) it was concluded that there was likely three, possibly four, pure component phases present in the Mn and Zn dataset. Multiple models were then evaluated relevant to the electrochemistry and phase evolution (see Tables S3 and S4, ESI†). The best model was determined based on the fit quality and the physical interpretability of the fitting result, the results of which are shown in Fig. S18 and S19 (ESI†).

The different components for the analysis included  $\beta$ -MnO<sub>2</sub>, MnSO<sub>4</sub> from the electrolyte and the reversible and irreversible Zn-Mn complexes. This 4-component model was tried but the spectra did not have a meaningful physical interpretation. Hence a three-component model for the operando XAS dataset across the Mn K-edge included a pristine β-MnO<sub>2</sub> spectra which was fixed during the fitting, along with two other references which were expected to be close to the Zn-Mn complex phases

and from the Mn<sup>2+</sup> ions in the liquid state or the layered ZHS structure formed as a result of the electrochemical process and the contributions of the electrolyte. These two components were allowed to vary. The two references were the 16th cycle charge electrode sample which could be represented by the irreversible complex and first cycle electrodeposited sample, which can be attributed to the Zn-Mn complex reversible complex (represented as the line spectra in Fig. 7A). The fit result is shown as the dotted spectra in Fig. 7A for the 16th cycle charge and electro-deposited sample respectively. The fitted concentration profiles (see Fig. 7B) show the relative concentration of MnO2 to gradually decrease throughout the experiment, as expected due to the dissolution, while one of the profiles increases during the discharge and decrease during the charge corresponding to the variation of the Mn<sup>2+</sup> ions coordination in the liquid state or the layered structure. The comparison of this fitted phase with the standard spectra for MnSO<sub>4</sub>,

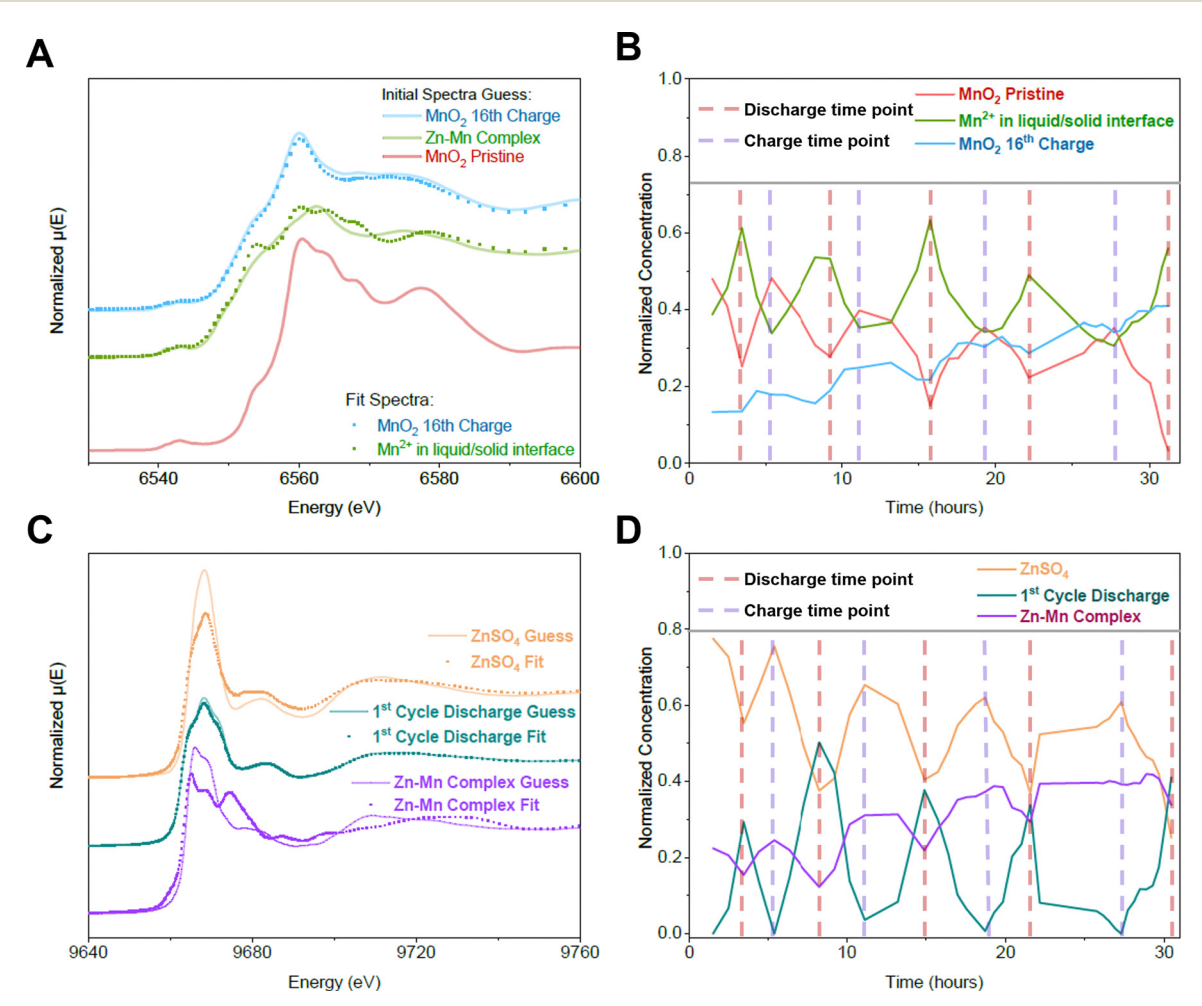


Fig. 7 MCR-ALS fitting of operando Mn and Zn XAS spectra to resolve the complex Mn-Zn phases. (A) The lines show the initial spectra guess consisting of  $MnO_2$  reference spectrum (red), Zn-Mn complex (green) and 16th Cycle charge sample  $\beta-MnO_2$  (blue) from the operando Mn XANES. The dotted spectra show the corresponding refined spectra after analysis. (B) Represents the corresponding fitted concentration profiles of the refined structure across the Mnedge with the dashed vertical lines indicating battery cycling between discharge and charge time points. (C) The lines show the initial spectra guess consisting of ZnSO<sub>4</sub> electrolyte, 1st cycle discharge sample (corresponding to the ZHS phase) and the Zn-Mn complex from the electrodeposited sample. The dotted spectra show the corresponding refined spectra after the MCR-ALS analysis. (D) Represents the corresponding fitted concentration profiles of the refined structure across the Zn-edge with the dashed vertical lines indicating battery cycling between discharge and charge time points.

This journal is © The Royal Society of Chemistry 2023

MnO,  $Mn^{3^+}$  ( $Mn_2O_3$ ) and  $Mn^{4^+}$  ( $\beta$ -MnO $_2$ ) is made in the Fig. S20 (ESI†) identifying the spectral contributions from the local ordering of  $Mn^{2^+}$  in the liquid/layered state. For the  $MnO_2$  16th cycle charge sample on observing the concentration profile, we attribute the reversible component (blue curve in Fig. 7B) to correspond to the reversible Zn–Mn complex and the increasing component to be the irreversible  $ZnMn_2O_4$  phase.

Additionally, a comparison between the  $MnO_2$  16th cycle charge fit spectra and the  $ZnMn_3O_7\cdot 2H_2O$  and  $ZnMn_2O_4$  spectra obtained from the FEFF analysis is made in Fig. S21 (ESI†). While the similarity between the  $ZnMn_2O_4$  and the fit spectra is visible, it is less evident with  $ZnMn_3O_7\cdot 2H_2O$ , which suggests the possibility of the formation of a different component during *operando* studies. Overall, the fact that Mn has an oxidation state of 3+ in  $ZnMn_2O_4$  and the reversible Zn-Mn component is amorphous with an oxidation state less than 4, indicates that the electrode, over long-term cycling, will eventually has an oxidation state between 3 and 4.

For the operando XAS dataset across the Zn absorption Kedge, the three-component model included the ZnSO<sub>4</sub> electrolyte (in liquid state), 1st cycle discharge sample (the Zn-species corresponds to the ZHS phase) and the Zn-Mn complex obtained from the electrodeposited sample. These three spectra are represented as the line spectra in Fig. 7C. The evolved spectra in Fig. 7C based on MCR analysis is represented by the dotted spectra. The fitted concentration profiles (see Fig. 7D) show that the relative concentration of ZnSO<sub>4</sub> electrolyte gradually decrease and increase throughout the discharge and charge process, while displaying an overall decreasing trend. On the contrary, the evolved 1st cycle discharge spectra increase and decrease during the discharge and charge process, indicating the reversibility of the ZHS phase. The evolved Zn-Mn complex phase gradually increases in concentration with increasing cycles and this phase is qualitatively similar to the ZnMn<sub>2</sub>O<sub>4</sub> phase (see Fig. 4F). The decrease in the relative ZnSO<sub>4</sub> concentration can be correlated to the increase in the irreversible ZnMn2O4 phase. Overall, the MCR-ALS analysis of the operando Zn dataset provides further evidence of the irreversible phase forming in the battery.

### 2.8 Proposed reaction mechanism and reasons for rise in pH

The overall schematic of the reaction mechanism is illustrated in Fig. 8 with the corresponding discharge and charge equations. The reactions specific to each region (1 to 3) is also represented by distinct colors yellow, dark blue and cyan color. In Fig. 8A the electrochemical potential is plotted as a function of the normalized relative wt of  $\beta$ -MnO $_2$  and ZHS component of Rietveld refinement of the *operando* X-ray diffraction studies for the first two and half cycles. During the discharge half-cycle, irreversible dissolution of  $\beta$ -MnO $_2$  contributes to the discharge capacity. As a result of the dissolution, the pH change at the interface leads to the precipitation of ZHS (yellow color, region 1, eqn (3) and (4)). This discharge process progresses with the consumption of 2 protons and 1 electron reaction. In the charge cycle an amorphous reversible Zn–Mn complex is formed by the proposed nucleation over the ZHS precipitates

as shown in eqn (5). The Mn in the amorphous phase can have an oxidation state of less than 4 (Z < 4 for Mn $^{Z^+}$ ). During this process the proton production may be less than 2 for every electron. In addition, a competing water oxidation may occur at potentials  $\sim 1.7$  V as shown in eqn (7) which may lead to the slight increase in overpotential in the charge half cycle. The reaction further produces one proton for every electron. This imbalance between the discharge and charge process can contribute towards the rise in pH observed in the charge half cycle specifically close to the potentials of  $\sim 1.7$  V.

During the subsequent discharge state the dissolution reaction mechanism of the amorphous phase including the proton consumption can be hypothesized to be a two step reaction. The first discharge curve may correspond to the gradual reduction of the amorphous phase by proton-diffusion through the amorphous phase (cyan color, region 2) followed by its dissolution in the flat region of the discharge curve leading to proton consumption and ZHS growth. This dissolution of the amorphous phase may further contribute towards proton consumption and hence lead to the formation of ZHS precipitate. This region of dissolution can be marked by the overlap between the cyan and yellow region. The dissolution of β-MnO<sub>2</sub> is marked by the dotted line under the MnO<sub>2</sub> wt fraction (in the yellow region 1). In addition, spontaneous reaction at the anode can be represented by the eqn (8) leads to the production of hydroxide ions.<sup>38</sup>

This cycling continues with the gradual increase in pH as a result of irreversible dissolution and spontaneous reactions in the battery leading to the irreversible precipitation of  $ZnMn_2O_4$  on the  $\beta$ -MnO<sub>2</sub> particles represented by eqn (6) further deteriorating the electrochemical activity of the electrode.

During long-term cycling both reactions for amorphous phase and the irreversible  $ZnMn_2O_4$  phase is hypothesized to be forming because of two components ( $Zn^{2+}$  and  $Mn^{2+}$ ) two phase (liquid to solid) reaction on ZHS or  $MnO_2$  active material and not by any intercalation reaction. Hence, the possibility of intercalation into  $\beta$ - $MnO_2$  after long term cycling is low.

$$MnO_{2(s)} + 4H^{^{+}} + Zn_{(s)} \rightarrow Mn_{(aq)}^{^{2+}} + 2H_{2}O_{(l)} + Zn_{(aq)}^{^{2+}} \ \, \big(3\big)$$

$$4Zn_{(aq)}^{2+} + SO_{4(aq)}^{2-} + 5H_2O_{(l)} + 6OH_{(aq)}^{-} \leftrightarrow Zn_4SO_4(OH)_6$$

$$5H_2O_{(s)} \qquad (4)$$

$$\operatorname{Mn_{(aq)}}^{2^{+}} + a\operatorname{Zn_{(aq)}}^{2^{-}} + x\operatorname{OH}^{-} + y\operatorname{H}_{2}\operatorname{O_{(l)}} + \leftrightarrow \operatorname{Zn}_{a}\operatorname{MnO}_{x}\cdot y\operatorname{H}_{2}\operatorname{O_{(s)}} + x\operatorname{H}^{+} + 2(x - a - 1)e^{-}$$
 (5)

$$Zn_{(aq)}^{2^{+}} + Mn_{(aq)}^{2^{+}} + MnO_{2(s)} + 2OH^{-} \rightarrow ZnMn_{2}O_{4(s)} + 2H^{+}$$
(6)

$$H_2O \rightarrow 2H_{(aq)}^+ + 0.5O_{2(aq/g)} + 2e^-$$
 (7)

$$Zn + 2H_2O \rightarrow H_2 + 2OH^-$$
 (8)

### 3. Conclusion

In this work, the dissolution–deposition mechanism of tunneled  $\beta$ -MnO<sub>2</sub> electrode coupled with Zn anode in mildaqueous electrolyte was thoroughly investigated using a

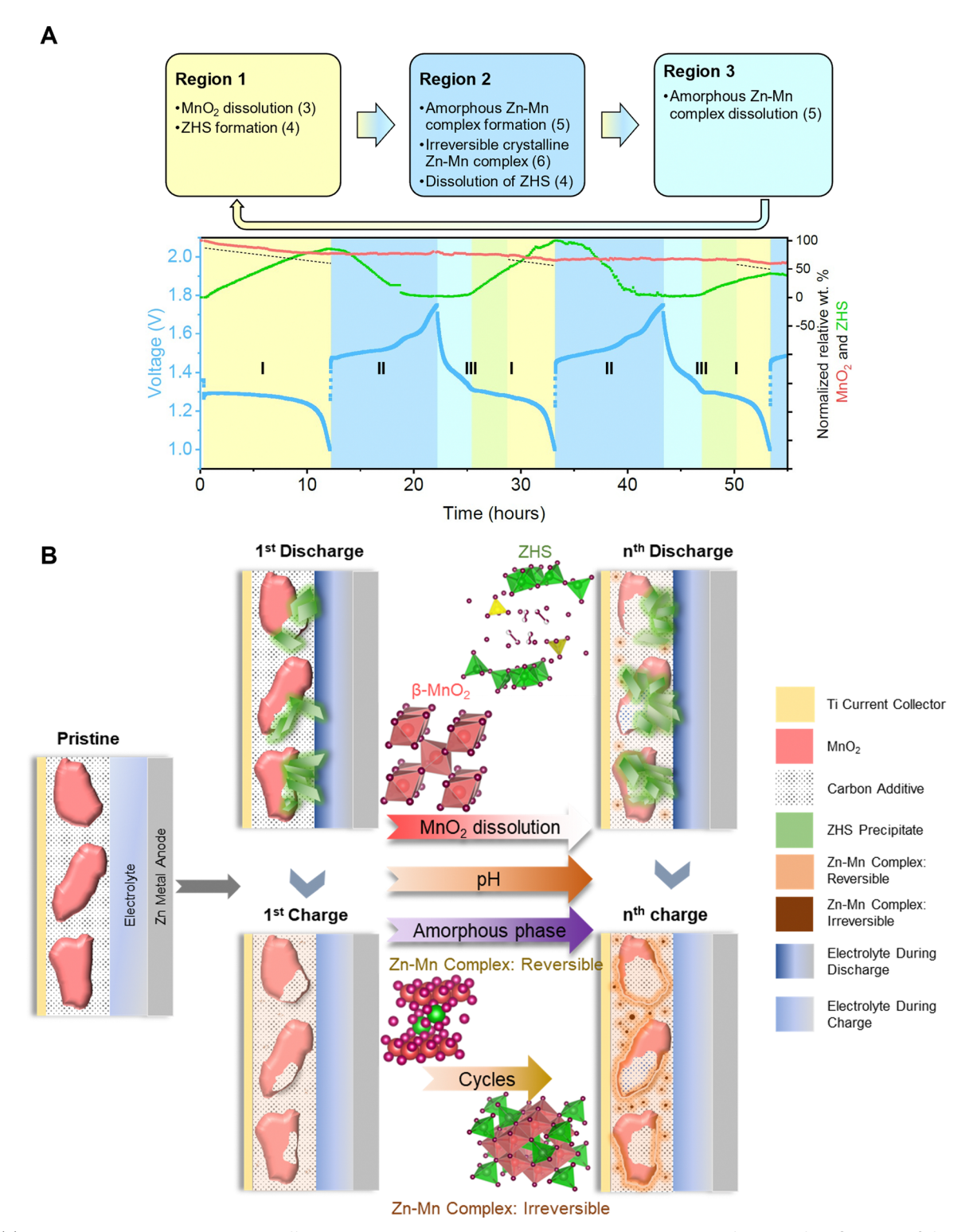


Fig. 8 (A) Proposed reaction mechanism at different voltage plateaus hypothesized by the normalized wt fraction of MnO2 and ZHS from Rietveld refinement and the key observations from this work. (B) Schematic illustration representing the irreversible dissolution of  $\beta$ -MnO<sub>2</sub> particles followed by precipitation of ZHS during discharge. The charge cycle is characterized by reversible amorphous phase growth over subsequent cycles forms overlapping phases leading to irreversibility and capacity fade.

combination of operando and ex situ synchrotron diffraction, spectroscopy, and microscopy techniques through a multimodal synchrotron approach.

The operando diffraction and absorption spectroscopy showed that the major capacity contribution during the first discharge cycle is due to the dissolution of MnO2 to Mn2+. The deposition of ZHS occurs, in the vicinity of the dissolution in parallel. This was visualized as a plate-like structure forming over the surface of  $MnO_2$  particles. Two Zn–Mn complexes phases deposit in the electrode upon charging, one is a reversible amorphous phase, and one is an irreversible crystalline phase.

In the initial charge half cycles, an amorphous Zn-Mn complex formed on the ZHS precipitate as it reversibly dissolved into the electrolyte. The capacity contribution in the following cycles is a combination of both dissolution of the amorphous phase and the remainder of the crystalline MnO<sub>2</sub> phase in the discharge and, the formation of the amorphous Zn-Mn complex phase during charging. Based on the Rietveld refinement of the operando X-ray diffraction scans, the lattice parameter, the crystallite size and the microscopic strain parameter were also evaluated. The negligible changes in the microscopic strain and lattice parameters supported the lack of intercalation in the system. Overall, a gradual change in operando and ex situ X-ray absorption spectra suggests loss of crystalline MnO2 species and an overall increase in the amorphous Zn-Mn complex. In addition to the reversible amorphous Zn-Mn complex phase, it is observed that there is a formation and growth of a spherical phase on the MnO2 particles in the charge state over increasing cycles. X-ray diffraction identified this irreversible Zn-Mn complex phase as a poorly crystalline ZnMn<sub>2</sub>O<sub>4</sub> (hetaerolite) phase. One of the reasons for this phase formation is attributed to the increase in pH of the electrolyte due to the increasing inhomogeneity in the battery thereby, leading to an increase in ZHS concentration.

Elementally sensitive nano-tomography using transmission X-ray microscopy on the battery over electrochemical cycling, demonstrated the colocalization of the Zn- and Mn-rich phases as Zn–Mn complexes, consistent with the X-ray diffraction and spectroscopy findings. These newly formed phases during cycling were further studied in *operando* X-ray fluorescence microscopy. Morphological analysis with 3D visualization of the 8th and 16th cycle charged state samples confirms that Zn–Mn complex phases form in the vicinity of MnO<sub>2</sub> particles. The later cycles, an increased amount of the irreversible Zn–Mn complex was observed, owing to the continuing build-up of the ZnMn<sub>2</sub>O<sub>4</sub> phase over the cycling.

Overall, the reasons for capacity fade are found to be the formation of the irreversible complex  $\rm ZnMn_2O_4$  (hetaerolite) phase and loss of integrity of electrode, both associated with the increase in pH of the electrolyte upon  $\rm MnO_2$  dissolution. Since  $\sim 25\%$  of the total mass of the active material dissolves in the first cycle, conventional slurry cast electrodes may not be suitable for  $\rm Zn/MnO_2$  batteries in mild-aqueous regime. Additionally, the redeposition of the amorphous phase may be preferential on the plate like morphology of ZHS which forms as an immediate result of the dissolution. A strategy to mitigate this is to use 3D nanostructured current collector or a high electronic conducting substrate and electrolyte modifications using additives to stabilize pH overall. The pH stabilization helps in stabilizing the amorphous phase stabilization, thereby

leading to improved battery performance. Based on the discussion with the β-MnO<sub>2</sub> electrode, regardless of the polymorph, as long as there is the dissolution of active material it will ultimately follow a similar reaction mechanism. Therefore, electrode architectures which would stabilize the deposition and dissolution of Zn-Mn amorphous phase can prove pivotal in battery designs with improved capacity and higher cycle life. One of the key findings in this study is that we showed the difference between operando and ex situ measurements of the Zn-Mn amorphous phase. The absence of ZnMn<sub>3</sub>O<sub>7</sub>·3H<sub>2</sub>O in the *operando* configuration, coupled with its appearance in the dried electrode, indicates that the compound previously thought to be the direct reaction product in the charge state, is actually a derived phase from unreacted Mn-ions present in the electrode. Overall, this work elucidates the mechanistic strategies to rationally design and enhance the overall performance of aqueous Zn-MnO2 batteries, with an emphasis on renewing the concept of taking advantage of the dissolutiondeposition mechanism for future energy-dense and sustainable energy storage system.

### 4. Materials and methods

# 4.1. Electrode preparation and electrochemical characterization

The β-MnO<sub>2</sub> electrode slurries were prepared by vortex-mixing the active material powders of  $\beta$ -MnO<sub>2</sub> ( $\geq$  99%, Sigma-Aldrich) with carbon black (Super C65, MTI Cooperation) and polyvinylidene fluoride (PVDF) binder (Alfa Aesar) in 1-methyl-2pyrrolidone (NMP) solvent (Alfa Aesar) through a planetary mixer (THINKY centrifugal mixer ARM-310, Thinky USA). The composition of the slurries was active material: carbon black: PVDF in a ratio of 70:20:10 by weight. The ratio of solids in the slurry to the NMP solvent is  $\sim 0.7$ . The slurry was casted onto 11.4 µm titanium foils (Goodfellow) with a doctor blade while the thickness of the electrode was controlled by the gap size of doctor blade to be at 100 µm. The casted electrodes were then subject to a drying process in a vacuum oven for 24 hours at a temperature of 60 °C and final thickness of the electrodes after drying was measured to be  $\sim 20 \mu m$ . The average mass loading of the electrodes used in this study is  $\sim 1.5 \text{ mg cm}^{-2}$ . The same electrode preparation protocol was used to prepare the battery cells tested in the laboratory and at the synchrotron beamlines.

To test the electrochemical performance of aqueous Zn–MnO $_2$  batteries, CR-2032 coin cells were assembled following the sequence of,  $\beta$ -MnO $_2$  cathode, Celgard 3500 separator, zinc anode (100  $\mu$ m in thickness), stainless steel spacer, and wave spring in ambient environment. The electrolyte used was 2 M ZnSO $_4$  + 0.1 M MnSO $_4$  and  $\sim$  45  $\mu$ L was used in each cell. The same electrolyte formulation was also used for the synchrotron characterizations as detailed in the later sections. Charge and discharge electrochemical tests were conducted using a Biologic VSP300 potentiostat with a voltage range of 1–1.75 V and 1.3–1.75 V. The C rates were defined by the mass of

 $MnO_2$  and experimental capacity of 150 mA h  $g_{MnO_2}^{-1}$ , based on electrochemical testing. Post-cycled scanning electron microscopy and energy dispersive spectroscopy maps were carried out on the electrodes with JEOL 7600 SEM at a bias of 15 keV and Preliminary X-ray diffraction of the electrodes were conducted using the Rigaku Smartlab Diffractometer at the Center for Functional Nanomaterials, Brookhaven National Laboratory.

4.1.1 Electro-deposition study on carbon black electrode. Coin-cells were assembled in a similar sequence as discussed in the previous section wherein instead of the β-MnO<sub>2</sub> cathode bare carbon black was used. The electrolyte used was 2 M  $ZnSO_4 + 0.1 \text{ M MnSO}_4$  and  $\sim 45 \mu L$  was used in each cell. The cells were first charged prior to discharge at a current density of  $4 \mu A cm^{-2}$ . Overall, the cell provides a capacity of 50 μA h cm<sup>-2</sup> which can be attributed to the 0.1 M MnSO<sub>4</sub> present in the electrolyte.

4.1.2 Vacuum filtrated β-MnO<sub>2</sub> on carbon cloth. The β-MnO<sub>2</sub> coated on CNT electrodes were prepared using a vacuum filtration method. 24 mg of β-MnO<sub>2</sub> and 6 mg of MWCNT (Sigma Aldrich) were dispersed in 6 mL of isopropyl alcohol by sonication for 2 hours. They were then mixed and sonicated again for another 30 min to form a uniform suspension. The suspension was filtered through an electrophilic carbon cloth (Fuel Cell Store) with filter paper (with a pore size of 450 nm), using vacuum filtration. The electrode was then dried in a vacuum oven at 60 °C for 2 hours. The average mass loading of these electrodes was  $\sim 4.5-5$  mg cm<sup>-2</sup>. For the synchrotron operando drying experiment the electrodes were placed in an acrylic cell between silicone gaskets with a Kapton window. 200 µL of 1 M ZnSO<sub>4</sub> was used as the electrolyte. Charge and discharge electrochemical tests were conducted using a Biologic VSP300 potentiostat with a voltage range of 1-1.75 V at a C-rate of C/5 based on the experimental capacity of 150 mA h.

### 4.2. Synchrotron characterization

4.2.1. Synchrotron X-ray diffraction studies of crystalline phase evolution. The X-ray diffraction experiments were conducted at the X-ray powder diffraction beamline (XPD, 28-ID-2) at National Synchrotron Light Source II (NSLS-II), Brookhaven National Laboratory (BNL). A 2D amorphous-silicon digital X-ray detector with 2048  $\times$  2048 pixels, pixel size 200  $\times$  200  $\mu m$ was utilized to collect the diffraction rings in transmission mode. The X-ray beam size was 0.5 mm  $\times$  0.5 mm. The diffraction rings in each 2D image were azimuthally integrated and reduced to an intensity vs.  $2\theta$  (diffraction angle) plot via a Python-based program DIOPTAS.35 To identify the corresponding phases, the peak profiles were first compared with the standard references provided by a commercial database including JADE and PDF-4+ 2020 (ICPDS-ICDD).

For operando X-ray diffraction experiments a coin-cell configuration was used with the observing window opened on the casing and spacer. The diameter of the window was 3 mm, and the window was sealed by Kapton film and epoxy. Two cells were measured simultaneously: (1) cycled between 1-1.75 V and (2) cycled between 1.3-1.75 V after an activation cycle between

1-1.75 V. The wavelength was 0.18456 Å (corresponding to an X-ray energy of 67.18 keV), where the sample to detector distance was first calibrated by using a CeO2 standard. The exposure time of each scan was 30 seconds per 2D diffraction pattern. Data was collected on each cell every 8 minutes cycled under a 0.1C rate.

The Rietveld refinements were then conducted using TOPAS-Academic V6 to obtain the evolution of the weight percentage of each phase, MnO2, ZHS and Ti, during the operando experiment. The weight percentages were normalized against the Ti weight percentage since Ti is electrochemically inactive and can serve as a reference for the operando measurement. The Ti had a slightly preferred orientation (PO) hence a correction was applied in the refinement.

Samples with selected conditions (see Table S1, ESI†) were also analyzed with ex situ synchrotron X-ray diffraction. To reduce preferred orientation effects, the powders from the coin cells at different electrochemical states were extracted from the current collector followed by sealing them with epoxy in Kapton capillaries. Each sample was measured during a rotation of 10 degrees per min relative to the incident X-ray beam. The X-ray beam size was 0.5 mm imes 0.5 mm. The wavelength was 0.1870 Å (corresponding to an X-ray energy of 66.3 keV), where the sample to detector distance was first calibrated by using a Ni standard. The exposure time of each scan was 60 seconds per 2D diffraction pattern. Samples for the operando drying experiment were measured in the transmission mode with X-ray wavelength of 0.1820 Å.

4.2.2. Synchrotron operando and ex situ X-ray absorption spectroscopic studies on chemical evolution. The X-ray absorption spectroscopy (XAS) experiment was conducted at the inner shell spectroscopy beamline (ISS, 8-ID), National Synchrotron Light Source II (NSLS-II) of Brookhaven National Laboratory (BNL). The ISS beamline utilizes a damping wiggler source that provides a high flux ( $\sim 5 \times 10^{13}$  ph s<sup>-1</sup>) and has an energy range from 4.9 keV to 36 keV, with a 0.5 mm  $\times$  0.5 mm  $(h \times v)$  spot size. The Mn and Zn K-edge absorption spectra were acquired by tuning a cryogenically cooled double crystal Si(111) monochromator, which enabled the energy fly-scanning mode. The spectra were recorded from the MnO2 electrode in the transmission and fluorescence modes. Scanning and data acquisition times were  $\sim 45$  seconds per spectrum.

For operando XAS experiments, a pouch cell configuration of  $25 \times 25$  mm active area was adopted with the observing window opened on the zinc anode. The diameter of the window was 5 mm. Up to 5 cells were run simultaneously under different cycling conditions. The pouch cells were cycled at a 0.2C rate. To mitigate potential beam damage, the operando XAS spectra were measured from a  $3 \times 3$  grid with a separation of 1 mm. The primary goal was to study the reaction mechanism beyond the initial stage of the reaction (later than three cycles), the spectra were collected at an interval of 1 hour for the first three cycles followed by intervals of 30 minutes for the fourth cycle and 15 minutes for the fifth cycle. At every time point, ten spectra were collected at the Mn K-edge and five spectra at the Zn K-edge; spectra from each time point were averaged for an adequate signal-to-noise ratio. The *ex situ* electrodes were prepared by extracting electrodes at different electrochemical states from the coin cells followed by immediate washing in HPLC grade water and drying in the vacuum for over 12 hours.

The Larch analysis package was used to batch process the *operando* spectra. Averaging the spectra and extracting time points were part of the batch process. The XAS data was also processed using the Demeter XAS Data Processing and Analysis software. The XAS spectra were normalized, and background subtracted in Athena; linear regression was used to fit the preedge region, and a quadratic polynomial was used to fit the post-edge region. The results were then sorted by the time-stamp and correlated with the electrochemical data collected during the *operando* experiments.

**4.2.3 Implementation of MCR-ALS for** *operando* **XAS measurement.** MCR-ALS is implemented in python *via* the pyMCR package developed by NIST. <sup>43</sup> pyMCR also implements several fitting constraints that help ensure physical interpretability of MCR-ALS fit results, such as non-negativity of absorption coefficients and concentration values as well as concentration sum-to-one. pyMCR is expanded upon in XView, a software package developed by Denis Leshchev of NSLS-II's ISS beamline (8-ID), which adds principal component analysis (PCA) and a graphical user interface (GUI) among other features. <sup>44</sup>

Using XView, MCR-ALS was applied to an *in situ* experimental dataset studying the material phase evolution at an MnO<sub>2</sub> electrode in (2 M ZnSO<sub>4</sub> + 0.1 M MnSO<sub>4</sub>) electrolyte during battery cycling. From scanning electron microscopy (SEM) and X-ray diffraction (XRD) analysis it was clear that new Zn–Mn complex phases were forming at the electrode surface, however the exact chemical nature of these phases was uncertain. Thus, MCR analysis, combined with SVD/PCA, was applied to the XANES region of XAS data around the Mn Kedge to gain better insight into the number of phases formed during the experiment and the chemistry of these phases.

From the SVD/PCA analysis as shown in the Fig. S16 and S17 (ESI†) it was concluded that there were likely three, though possibly four, pure component phases present in the operando Mn and Zn datasets. This conclusion was based on several aspects of the SVD/PCA. First, the fourth principal component (PC) is less smooth than the first three, implying that this component begins to describe the experimental noise in the dataset rather than important spectral features. Second, the scree plot, which essentially plots the importance of each PC by its singular value and chi-square value, begins to level off around four PCs. Finally, the autocorrelation of the fourth eigen-concentration profile is significantly lower than the first three. Autocorrelation is a measurement of the degree to which changes in a value are correlated with previous changes. This is a valuable metric for XAS PCA since we do not expect drastic changes in any spectral features from one measurement to another. Therefore, a low autocorrelation for the concentration profile of a XAS PC can indicate that the PC is mostly describing noise in the dataset.

4.2.4 FEFF to simulate the XANES spectra of Zn-Mn complex phases. Simulation of the XANES spectra for ZnMn<sub>3</sub>O<sub>7</sub>·3H<sub>2</sub>O and ZnMn<sub>2</sub>O<sub>4</sub> were calculated using the FEFF 10 code to study the spectra similarities in the pre and post edge features with the experimentally measured XANES spectra. FEFF is a program for *ab initio* multiple scattering calculations using the full multiple scattering (FMS) theory within muffintin approximation. 30,31 The crystal structures for ZnMn<sub>3</sub>O<sub>7</sub>· 3H<sub>2</sub>O (PDF #04-011-5216) and ZnMn<sub>2</sub>O<sub>4</sub> (PDF #04-002-4954) were obtained from the cif files from the standard crystal database. A cluster with a radius of 30 Å was generated using the ATOMS program. The XANES spectrum for this cluster was calculated using a maximum k value of 12.0, step size of  $0.07 \text{ Å}^{-1}$  and an amplitude reduction factor 0.9. The FMS was calculated for a cluster size of 8 Å and the self-consistent field (SCF) potential calculated for 4 Å. The SCF parameter was used to determine the convergence for the self-consistency loop. The obtained spectra were shifted in energy to make appropriate comparison with the experimentally obtained spectra.

4.2.5. Synchrotron X-ray nano-tomography to study the morphological evolution. The synchrotron nanoimaging study was conducted at the full-field X-ray imaging beamline (FXI, 18-ID) of National Synchrotron Light Source II (NSLS-II) at the Brookhaven National Laboratory. The X-ray incident energy used was 7.09 and 6.41 keV which corresponds to above and below Mn K-edge (6.539 keV), and 9.8 and 9.53 keV which corresponds to above and below Zn K-edge (9.659 keV), providing optimal imaging contrast for the Mn and Zn complex phases. The images from the Transmission X-ray Microscope (TXM) at FXI Beamline were captured using a lens-coupled CCD detector with 2560  $\times$  2160 pixels has a field of view of 46.8  $\mu m \times 55.48 \ \mu m \ (h \times \nu)$  field of view. A camera binning of 2  $\times$  2 was used, resulting in an effective pixel size of 43.34 nm.

The electrodes at different electrochemical states were cut into a wedge shape with a tip size less than 50  $\mu$ m and then mounted on a stainless-steel pin with epoxy. For each tomography scan the exposure time and rotation speed were tuned such that we could capture  $\sim 900$  projections, with a total acquisition time of 1–1.5 minute per scan. The tomography projections were low pass filtered before reconstruction with the Gridrec algorithm, which was done with Tomopy.  $^{45,46}$ 

The 3D tomographic reconstruction stack images at the four energies were rotated and cropped into suitable volumes using the TransformJ rotate and Crop3D plugins in the FIJI package of ImageJ. This was followed by a volume registration conducted in Tomviz. If for each sample, the below absorption edge image was then subtracted from the above edge image to obtain volumetric image stacks with improved contrast on selected phases (Mn-rich and Zn-rich, for the corresponding edges). Following this, the 2D virtual cross-section images and 3D morphological evolution was conducted employing the commercial software Avizo (Thermo Fisher Scientific, v9.3) on the final image stacks.

**4.2.6. Synchrotron X-ray fluorescence microscopy to study the elemental distribution.** The *operando* X-ray fluorescence microscopy (XRF) experiment was conducted at the sub-micron

resolution X-ray spectroscopy beamline (SRX, 5-ID) at NSLS-II. The incident X-ray energy was 15 keV, focused onto the sample by a set of Kirkpatrick-Baez mirrors with a spot size of  $\sim 0.5$ μm. XRF experiment was conducted by raster scanning the sample against the incident X-ray beam, and the full XRF spectrum from the sample at each scanned point (pixel) was collected by a silicon drift detector. During the operando XRF experiment, the Zn-MnO<sub>2</sub> coin cell was discharged and charged at C/5 rate. The operando setup included a coin-cell battery with a Kapton window and the XRF scans were collected on the cathode side of the battery with each  $60 \times 60 \mu m$  image taking  $\sim$  20 min. The elemental distribution evolution can be obtained using XRF microscopy by fitting the fluorescence spectra using the PyXRF software.49

### **Author contributions**

V. R. K., N. Z., M. G. and Y.-C. K. C.-W. developed the research idea. V. R. K., N. Z., C.-H. L., J. B., H. Z., S. G., and Y.-C. K. C.-W. designed the synchrotron X-ray diffraction experiments. V. R. K., N. Z. conducted the synchrotron diffraction measurements with the XPD beamline staff H. Z., J. B. and S. G. V. R. K. performed the diffraction data analysis under the guidance of J. B., H. Z., and Y.-C. K. C.-W. V. R. K., N. Z., D. L., E. S., and Y.-C. K. C.-W. designed synchrotron X-ray absorption spectroscopy experiments. V. R. K., N. Z., Y.-C. K. C.-W. conducted the synchrotron absorption spectroscopy measurements with the ISS beamline staff D. L. and E. S. V. R. K., C.-H. L., and N. Z. performed the XANES data analysis and V. R. K. conducted the EXAFS data analysis, both under the guidance of D. L., E. S., and Y.-C. K. C.-W. C. C. and V. R. K. conducted the MCR-ALS analysis under the guidance of D. L., E. S. V. R. K., N. Z., X. Z., C.-H. L., Y.-C. K. C.-W. conducted the synchrotron imaging experiments with the FXI beamline staff M. G. V. R. K., X. Z. and N. Z. performed synchrotron imaging data analysis under the guidance of M. G. and Y.-C. K. C.-W. V. R. K., X. Z., N. Z. and Y.-C. K. C.-W. designed and conducted the synchrotron fluorescence imaging experiments with the SRX beamline staff A. K. X. Z. and V. R. K. performed the SRX data analysis under the guidance of Y.-C. K. C.-W. V. R. K. and N. Z. prepared the MnO2 electrodes, assembled the electrochemical cells and performed morphological analysis by SEM. V. R. K. conducted the laboratory X-ray diffraction measurement and analysis under the guidance of D. N. V. R. K. wrote the manuscript under the supervision of Y.-C. K. C.-W. and inputs from K. J. T., A. C. M. and E. S. T., as well as all coauthors.

### Conflicts of interest

The authors declare no competing financial interest.

## Acknowledgements

This research was supported by the Center for Mesoscale Transport Properties, an Energy Frontier Research Center supported by the U.S. Department of Energy, Office of Science, Basic Energy Sciences, under award #DE-SC0012673. This research used resources, X-ray Powder Diffraction beamline (XPD, 28-ID-2), Inner-Shell Spectroscopy beamline (ISS, 8-ID), Full Field X-ray Imaging beamline (FXI, 18-ID), Beamline for Materials Measurement (BMM, 6-BM) and Submicron Resolution X-ray Spectroscopy beamline (SRX, 5-ID) of the National Synchrotron Light Source II, a U.S. Department of Energy (DOE) Office of Science by Brookhaven National Laboratory under Contract No. DE-SC0012704. This research used Materials Synthesis and Characterization Facility of the Center for Functional Nanomaterials (CFN), which is a U.S. Department of Energy Office of Science User Facility, at Brookhaven National Laboratory under Contract No. DE-SC0012704. Partial support for Nicole Zmich was provided by an NSF NRT Award in Quantitative Analysis of Dynamic Structures (DGE 1922639) as a fellowship. We are grateful for the helpful feedback and discussion with the m2M#s center members. We are also thankful to beamline scientist, Dr Bruce Ravel for his extensive support during the BMM beamtime. We acknowledge the support on data collection during beamtime, preliminary analysis, and discussion provided by Chen-Wiegart group members, Arthur Ronne, Xiaoyang Liu, and Dean Yen. We thank the support of Data Sci & System Integration staff, Steven LaMarra and XPD beamline staff, John Trunk, both at NSLS-II, for setting up the operando diffraction experiment. We thank the beamline scientists Dr Wah-Keat Lee and Dr Xianghui Xiao from FXI beamline research and development. We also thank the support provided by the CFN staff, Gwen Wright and for the access and training on FE-SEM. EST acknowledges the support of the William and Jane Knapp Chair of Energy and the Environment.

### References

- 1 T. M. Gür, Energy Environ. Sci., 2018, 11, 2696-2767.
- 2 D. Larcher and J. M. Tarascon, Nat. Chem., 2015, 7, 19-29.
- 3 M. Song, H. Tan, D. Chao and H. J. Fan, Adv. Funct. Mater., 2018, 28, 1802564.
- 4 L. E. Blanc, D. Kundu and L. F. Nazar, Joule, 2020, 4, 771-799.
- 5 K. Kordesch, J. Gsellmann, M. Peri, K. Tomantschger and R. Chemelli, Electrochim. Acta, 1981, 26, 1495-1504.
- 6 H. Pan, Y. Shao, P. Yan, Y. Cheng, K. S. Han, Z. Nie, C. Wang, J. Yang, X. Li, P. Bhattacharya, K. T. Mueller and J. Liu, Nat. Energy, 2016, 1, 16039.
- 7 S. Islam, M. H. Alfaruqi, V. Mathew, J. Song, S. Kim, S. Kim, J. Jo, J. P. Baboo, D. T. Pham, D. Y. Putro, Y.-K. Sun and J. Kim, J. Mater. Chem. A, 2017, 5, 23299-23309.
- 8 B. Lee, C. S. Yoon, H. R. Lee, K. Y. Chung, B. W. Cho and S. H. Oh, Sci. Rep., 2014, 4, 6066.
- 9 W. Sun, F. Wang, S. Hou, C. Yang, X. Fan, Z. Ma, T. Gao, F. Han, R. Hu, M. Zhu and C. Wang, J. Am. Chem. Soc., 2017, 139, 9775-9778.
- 10 J. Wang, J.-G. Wang, H. Liu, C. Wei and F. Kang, J. Mater. Chem. A, 2019, 7, 13727-13735.

- 11 D. R. Wu, L. M. Housel, S. J. Kim, N. Sadique, C. D. Quilty, L. J. Wu, R. Tappero, S. L. Nicholas, S. Ehrlich, Y. M. Zhu, A. C. Marschilok, E. S. Takeuchi, D. C. Bock and K. J. Takeuchi, Energy Environ. Sci., 2020, 13, 4322-4333.
- 12 L. Wang and J. Zheng, Mater. Today Adv., 2020, 7, 100078.
- 13 M. Mateos, K. D. Harris, B. Limoges and V. Balland, ACS Appl. Energy Mater., 2020, 3, 7610-7618.
- 14 H. Moon, K. H. Ha, Y. Park, J. Lee, M. S. Kwon, J. Lim, M. H. Lee, D. H. Kim, J. H. Choi, J. H. Choi and K. T. Lee, Adv. Sci., 2021, 8, 2003714.
- 15 J. Lei, Y. Yao, Z. Wang and Y.-C. Lu, Energy Environ. Sci., 2021, 14, 4418-4426.
- 16 S. J. Kim, D. Wu, N. Sadique, C. D. Quilty, L. Wu, A. C. Marschilok, K. J. Takeuchi, E. S. Takeuchi and Y. Zhu, Small, 2020, 16, 2005406.
- 17 T. N. T. Tran, S. Jin, M. Cuisinier, B. D. Adams and D. G. Ivey, Sci. Rep., 2021, 11, 20777.
- 18 H. Chen, C. Dai, F. Xiao, Q. Yang, S. Cai, M. Xu, H. J. Fan and S.-J. Bao, Adv. Mater., 2022, 34, 2109092.
- 19 S.-M. Bak, Z. Shadike, R. Lin, X. Yu and X.-Q. Yang, NPG Asia Mater., 2018, 10, 563-580.
- 20 Y.-C. K. Chen-Wiegart, I. Waluyo, A. Kiss, S. Campbell, L. Yang, E. Dooryhee, J. R. Trelewicz, Y. Li, B. Gates, M. Rivers and K. G. Yager, Synchrotron Radiation News, 2020, 33, 44-47.
- 21 C. Zhao, K. Kisslinger, X. Huang, M. Lu, F. Camino, C.-H. Lin, H. Yan, E. Nazaretski, Y. Chu, B. Ravel, M. Liu and Y.-C. K. Chen-Wiegart, Mater. Horiz., 2019, 6, 1991-2002.
- 22 C.-H. Lin, L. Wang, S. T. King, J. Bai, L. M. Housel, A. H. McCarthy, M. N. Vila, H. Zhu, C. Zhao, L. Zou, S. Ghose, X. Xiao, W.-K. Lee, K. J. Takeuchi, A. C. Marschilok, E. S. Takeuchi, M. Ge and Y.-C. K. Chen-Wiegart, ACS Cent. Sci., 2021, 7, 1676–1687.
- 23 D. Atkins, E. Capria, K. Edström, T. Famprikis, A. Grimaud, Q. Jacquet, M. Johnson, A. Matic, P. Norby, H. Reichert, J. P. Rueff, C. Villevieille, M. Wagemaker and S. Lyonnard, Adv. Energy Mater., 2022, 12, 2102694.
- 24 N. Zhang, F. Cheng, J. Liu, L. Wang, X. Long, X. Liu, F. Li and J. Chen, Nat. Commun., 2017, 8, 405.
- 25 M. Chamoun, W. R. Brant, C.-W. Tai, G. Karlsson and D. Noréus, Energy Storage Mater., 2018, 15, 351-360.
- 26 B. H. Toby, Powder Diffr., 2006, 21, 67-70.
- 27 S. Dolabella, A. Borzì, A. Dommann and A. Neels, Small Methods, 2022, 6, 2100932.
- 28 Y. Li, S. Wang, J. R. Salvador, J. Wu, B. Liu, W. Yang, J. Yang, W. Zhang, J. Liu and J. Yang, Chem. Mater., 2019, 31, 2036-2047.

- 29 K. R. Tallman, G. P. Wheeler, C. J. Kern, E. Stavitski, X. Tong, K. J. Takeuchi, A. C. Marschilok, D. C. Bock and E. S. Takeuchi, J. Phys. Chem. C, 2021, 125, 58-73.
- 30 X. Gao, H. Wu, W. Li, Y. Tian, Y. Zhang, H. Wu, L. Yang, G. Zou, H. Hou and X. Ji, Small, 2020, 16, 1905842.
- 31 E. Castorina, E. D. Ingall, P. L. Morton, D. A. Tavakoli and B. Lai, J. Synchrotron Radiat., 2019, 26, 1302-1309.
- 32 J. J. Rehr, J. J. Kas, F. D. Vila, M. P. Prange and K. Jorissen, Phys. Chem. Chem. Phys., 2010, 12, 5503-5513.
- 33 J. J. Kas, F. D. Vila, C. D. Pemmaraju, T. S. Tan and J. J. Rehr, J. Synchrotron Radiat., 2021, 28, 1801-1810.
- 34 Y.-c K. Chen-Wiegart, J. S. Cronin, Q.-x Yuan, K. J. Yakal-Kremski, S. A. Barnett and J. Wang, J. Power Sources, 2012, **218**, 348–351.
- 35 C. Prescher and V. B. Prakapenka, High Press. Res., 2015, 35, 223-230.
- 36 L. Li, T. K. A. Hoang, J. Zhi, M. Han, S. Li and P. Chen, ACS Appl. Mater. Interfaces, 2020, 12, 12834-12846.
- 37 J. C. Knight, S. Therese and A. Manthiram, J. Mater. Chem. A, 2015, 3, 21077-21082.
- 38 D. Perez-Antolin, I. Sáez-Bernal, A. Colina and E. Ventosa, Electrochem. Commun., 2022, 138, 107271.
- 39 A. Martini and E. Borfecchia, Crystals, 2020, 10, 664.
- 40 C. F. Bischoff, O. S. Fitz, J. Burns, M. Bauer, H. Gentischer, K. P. Birke, H.-M. Henning and D. Biro, J. Electrochem. Soc., 2020, 167, 020545.
- 41 M. Newville, J. Phys.: Conf. Ser., 2013, 430, 012007.
- 42 B. Ravel and M. Newville, J. Synchrotron Radiat., 2005, 12, 537-541.
- 43 C. H. Camp, Jr., J. Res. Natl. Inst. Stand. Technol., 2019, 124, 1-10.
- 44 D. Leshchev, M. Rakitin, B. Luvizotto, R. Kadyrov, B. Ravel, K. Attenkofer and E. Stavitski, J. Synchrotron Radiat., 2022, 29, 1095-1106.
- 45 D. A. Gürsoy, F. De Carlo, X. Xiao and C. Jacobsen, J. Synchrotron Radiat., 2014, 21, 1188-1193.
- 46 A. D. Betsy, H. C. Graham, B. M. Robert, V. N. Vivek, V. T. Sameer, A. Lisa and D. P. Siddons, Proc. SPIE, 1999, 3772, 224-236.
- 47 C. A. Schneider, W. S. Rasband and K. W. Eliceiri, Nat. Methods, 2012, 9, 671–675.
- 48 R. Hovden, M. D. Hanwell, U. Ayachit, Y. Jiang, R. Maynard and D. A. Muller, Microsc. Microanal., 2015, 21, 2407-2408.
- 49 L. Li, H. Yan, W. Xu, D. Yu, A. Heroux, W.-K. Lee, S. Campbell and Y. Chu, PyXRF: Python-based X-ray fluorescence analysis package, SPIE, 2017.